Geophys. J. Int. (2004) **158,** 109–130 doi: 10.1111/j.1365-246X.2004.02305.x

Three-dimensional upper-mantle *S*-velocity model for the Eurasia–Africa plate boundary region

Federica Marone,* Suzan van der Lee† and Domenico Giardini

Institute of Geophysics, ETH-Hönggerberg, CH-8093 *Zurich, Switzerland. E-mail: federica@seismo.berkeley.edu*

Accepted 2004 January 28. Received 2004 January 28; in original form 2003 September 22

SUMMARY

A new regional *S*-velocity study resolving the Eurasia–Africa plate boundary region from the Azores to the eastern Mediterranean Sea is presented. The resolution of existing velocity models has been complemented by using new seismic broad-band data recorded by the temporary MIDSEA network and at permanent European seismic stations. Following the partitioned waveform inversion method, we interactively fitted the waveforms of *S* and Rayleigh wave trains of more than 1100 seismograms. The linear constraints on upper-mantle *S* velocity provided by the waveform fits have been combined with independent estimates of Moho depth in a linear damped least-squares inversion for *S* velocity and crustal thickness. The resulting *S*-velocity structure for the Mediterranean Sea shows strong lateral variations, confirming the complex evolution of this plate boundary region. The upper mantle along the Eurasia–Africa suture zone is characterized by high-velocity material representing subducted oceanic lithosphere. This signature can be followed to depths of 300–500 km, depending on the region and resolution. A high-velocity body, possibly representing a fragment of subducted lithosphere, has been imaged beneath eastern Spain at a depth between 250 and 500 km. Not only convergence has been recorded in the upper mantle, but extension also has its own signature beneath the Mediterranean region. This is particularly clear for the Algero-Provençal and Tyrrhenian basins, where a shallow asthenospheric layer is observed. The lithosphere–asthenosphere system of the western Mediterranean clearly differentiates itself from the structure of the older eastern Atlantic Ocean. Differences in comparison to the structure of a 4 to 20 Ma ocean are also present. These observations support the idea that, rather than a young ocean, the western Mediterranean could be a strongly stretched continent, partly affected by spreading, formed at the back of a slab. The structure characterizing the eastern Mediterranean points to a continuation of the northern African continental lithosphere beneath the sea. Major structural differences in the eastern Atlantic Ocean are imaged between the mid-Atlantic ridge and the older oceanic basins: the north Atlantic lithosphere is characterized by lower velocities beneath the spreading ridge than under the old ocean basins. Despite the strong differences observed in the crustal structure between the mid-Atlantic ridge and the Azores, no significant differences are observed in the *S*-velocity structure of the upper mantle.

Key words: broad-band, mantle structure, Mediterranean, Rayleigh waves, shear wave velocity, waveform analysis.

1 INTRODUCTION

The Mediterranean region is characterized by the plate boundary between the Eurasian and African plates, extending from the Azores triple junction to Turkey and the easternmost Mediterranean Sea. Convergence of these two large continental plates makes this a tectonically complex region showing strong lateral variations in past and present dynamics.

Fundamental for a deeper understanding of the evolution, deformation and dynamics of such a complex region is a detailed knowledge of its 3-D upper-mantle structure. For example, a 3-D velocity model can reveal differences in the nature of the Mediterranean basins, anomalies associated with mid-oceanic ridges, styles of past subduction, the presence and extent of low-rigidity parts

*Now at: Berkeley Seismological Laboratory, University of California, 215 McCone Hall, Berkeley, CA 94720, USA.
†Now at: Department of Geological Sciences, Northwestern University, 1850 Campus Drive, Evanston, IL 60208, USA.

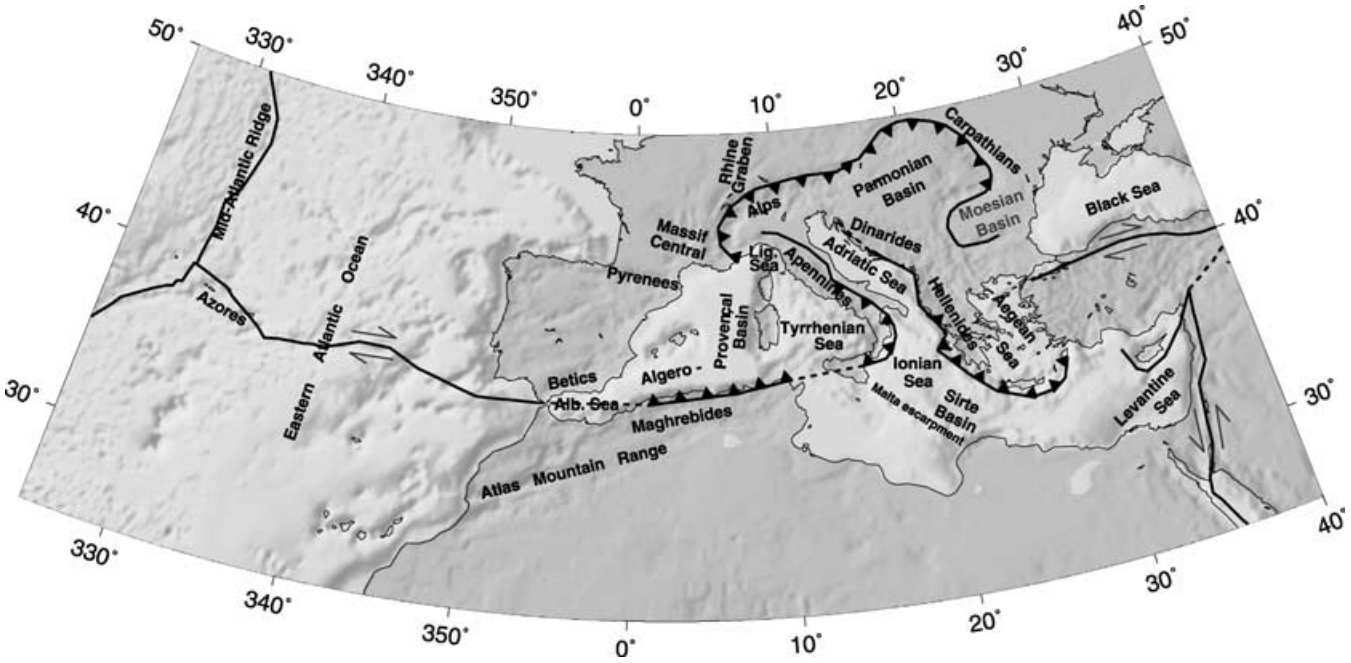

Figure 1. Topographic map of the Eurasia–Africa plate boundary region with approximate location of the plate boundary. Curves with a sawtooth pattern indicate the present location of the convergent boundary, with sawteeth pointing in the direction of subduction or underthrusting. Transcurrent boundaries are represented by arrows.

of the mantle, differences in oceanic and continental lithosphere–asthenosphere systems and the configuration of subducted lithosphere. This type of additional information about the ongoing processes is also necessary for advanced seismic and volcanic hazard assessment in the highly populated Mediterranean region. Moreover, a detailed velocity model is important for reducing uncertainties in earthquake location and determination of focal mechanisms, in particular in highly heterogeneous regions, as for instance along a plate boundary.

Current models for the Mediterranean region are incomplete due to inhomogeneous data distribution. To improve the data coverage, 25 broad-band three-component seismic stations have been deployed during the international project MIDSEA (Mantle Investigation of the Deep Suture between Eurasia and Africa) (Van der Lee *et al.* 2001). Most stations have been installed on Mediterranean islands or along the northern African coast and complement data coverage provided by existing networks and stations in the region.

In this study we combine new surface wave data recorded by the MIDSEA network with data from permanent broad-band seismic stations to derive a 3-D upper-mantle *S*-velocity model for the Mediterranean region. Our model covers the Eurasia–Africa plate boundary region from the Azores to the eastern Mediterranean Sea.

1.1 Tectonic background

The Eurasia–Africa plate boundary does not manifest itself as a sharp contact zone, but surface deformation, seismicity and earthquake focal mechanisms indicate a wide, diffuse and/or branched plate boundary. Owing to the formation and amalgamation of several semi-independent microcontinents between the two major plates, the plate boundary has changed location, shape and character throughout geological time (Dercourt *et al.* 1986). Despite slow convergence acting as the primary tectonic process in the region, extension, strike-slip and thrusting affect and have affected different parts of the plate boundary. Unique to the Mediterranean region is the small scale of complexity: typical lengths of the tectonic provinces span 1–5° (Fig. 1).

The complex tectonic evolution of the plate boundary is described in detail in, for example, Dercourt *et al.* (1986), Dewey *et al.* (1989) and De Jonge *et al.* (1994) and references therein. The history of the Mediterranean region is governed by the creation and subsequent destruction of the Tethys Ocean. After an early period dominated by extension and formation of oceanic lithosphere along different ridge systems, coincident with the breaking up of the Pangea landmasses (Jurassic–Cretaceous boundary), convergence has been acting as the primary plate tectonics process. About 65 Ma (Cretaceous–Tertiary boundary), following the opening of the Atlantic Ocean, the European and African plates started to converge. Formation of oceanic lithosphere in the region stopped and subduction and thrusting processes occurred along the entire northern Tethys margin. This convergence is responsible for the present-day mountain belts: Pyrenees, Betic Cordillera, Alps, Apennines, Carpathians, Dinarides and Hellenides. Small and large portions of the oceanic lithosphere have subducted beneath the volcanic-arc predecessors of many of these mountain belts. Parts of the original oceanic lithosphere (100 Ma) might still be preserved nowadays in the eastern Mediterranean Sea (e.g. the Levantine Basin). Recently, several backarc basins were created mainly in the western Mediterranean Sea by rapid extensional activity (Algero-Provençal Basin (30–16 Ma), Tyrrhenian (10–0 Ma) and Aegean Sea (30–0 Ma)).

1.2 Previous studies

The upper-mantle 3-D velocity structure of the Mediterranean area has been the subject of several tomographic studies. However, a detailed and complete image of the entire Eurasia–Africa suture zone has not yet been achieved. Existing models are either too local

or patchy, or show too long a wavelength character inadequate to resolve features on Mediterranean scales.

Traveltime tomographic models, such as the global *P*-velocity model of Bijwaard & Spakman (2000) or the regional *P*-velocity studies for example by Spakman *et al.* (1993) and Piromallo & Morelli (2003), do not resolve structures of the shallow mantle beneath the Mediterranean Basin. This is a consequence of lack of earthquakes and seismic stations in the sea and on the northern African coast and of the body waves travelling quasi-vertically through the lithosphere, leading to vertical leaking of the anomalies. The insufficient resolution of body wave tomographic models for the shallow mantle beneath aseismic regions covered by water has been documented for example by Spakman *et al.* (1993). Moreover, owing to the different sensitivity of *P*, *S* and surface waves, our velocity model will emphasize different structures than *P*-wave tomographic studies. For instance the conditions that decrease wave velocities, such as high mantle temperature, occurrence of melts and/or fluids or chemical composition, have a significantly larger effect on *S* rather than on *P* velocities (Cammarano *et al.* 2003). Therefore, locations where these conditions exist are more easily detected using *S* and surface waves.

Recent global studies that involve the inversion of surface wave data (e.g. Boschi 2001; Shapiro & Ritzwoller 2002) clearly image the long-wavelength structure of the Mediterranean region but are still inadequate to describe its complex upper mantle.

Regional surface wave studies for the Mediterranean region were introduced by Panza *et al.* (1980), who presented the first maps outlining the regionalization of the crust and lithosphere–asthenosphere system in the western and central Mediterranean. Snieder (1988) inverted waveforms of fundamental mode Rayleigh waves and their coda for a two-layered lateral model of *S* velocities in the upper 200 km of the mantle. Zielhuis & Nolet (1994) presented a 3-D *S*-velocity model for Europe and part of the Mediterranean region. However, they observed that surface wave analysis around the plate boundary region suffers from the structural complexity, which could not be adequately modelled for a lack of closely distributed seismic stations. Zielhuis & Nolet (1994) show a map of wave paths for which the waveform fits were poor: the map is dominated by Mediterranean paths, often longer than 20°, while the typical length of tectonic provinces in the region spans 1–5°. Marquering & Snieder (1996) did not improve the path coverage for the Mediterranean region relative to that of Zielhuis & Nolet (1994). Martínez *et al.* (2000) presented a 3-D *S*-velocity model focused on the Mediterranean Basin. However, their model is based on a limited set of available seismograms and on only fundamental mode Rayleigh waves. Moreover, a geodynamic interpretation of their results is not yet possible since the spatial resolution of their data set is still unpublished.

Higher-resolution regional studies tend to focus on a specific region within the Mediterranean Basin. Among others, Papazachos & Nolet (1997) have resolved the high-velocity structure of the subducting African Plate in the mantle beneath the Aegean region using *P*- and *S*-wave traveltimes. Southern Spain and the Alboran Sea have also been the target of several tomographic studies. Here, a high-velocity body has been imaged in the mantle between 200 and 700 km. Blanco & Spakman (1993) interpreted this anomaly as subducted lithosphere, possibly detached from the surface. The upper mantle beneath the Italian peninsula has also been the object of intensive investigations (e.g. Lucente *et al.* 1999).

Only few *S*-velocity studies exist for northern Africa. Ritsema & Van Heijst (2000) presented a regional model for the whole of Africa, focusing on gross features such as cratons and the East African Rift, while short-wavelength structures typical of the Mediterranean region are averaged out.

2 METHOD

We apply the version of partitioned waveform inversion (PWI) described by Van der Lee & Nolet (1997). Here we use PWI to image the 3-D *S*-velocity upper-mantle structure of the Mediterranean region using vertical and radial component seismograms recorded at European and northern African broad-band seismic stations. In addition to the 3-D *S*-velocity model presented here (EAV03), this application has also yielded a map for the Moho discontinuity (EAM02, Fig. 2), which has been discussed separately (Marone *et al.* 2003).

In the first part of PWI, the 1-D average *S*-velocity structure and Moho depth along each path are determined by non-linear waveform fitting of wave trains composed of fundamental and higher-mode surface waves. In the second part, the path average velocity structures obtained from waveform fitting and independent point constraints on Moho depth are combined in a damped linear inversion for 3-D *S* velocity and crustal thickness.

2.1 Waveform modelling

We obtained path average 1-D *S*-velocity models by fitting synthetic seismograms to observed waveforms. This fitting is done through minimization of the objective function $F(\gamma)$ making use of a non-linear optimization method based on conjugate gradients (Nolet 1990):

$$F(\gamma) = \int w^2(t)[\boldsymbol{R}d(t) - \boldsymbol{R}s(t,\gamma)]^2\,dt \qquad (1)$$

where $d(t)$ is the recorded and $s(t, \gamma)$ the synthetic seismogram, which depends on the model parameters γ. $\boldsymbol{R}$ is a filtering and windowing operator and $w(t)$ a weighting function based on the inverse of the signal envelope, to enhance the contribution to the misfit of the higher modes with respect to the naturally dominating fundamental mode.

We constructed synthetic seismograms by summation of the first 20 Rayleigh mode branches, with phase velocities between 2 and 10 km s^{-1}. We take into account the dependence of the partial derivatives of phase velocity over *S* velocity on Earth structure by using for each path a 1-D starting model that approximates the average structure along that path. Important aspects of these models are the depth of the Moho and the presence of a water layer. For continental paths, models similar to iasp91 (Kennett & Engdahl 1991) with different crustal thicknesses (ranging from 20 to 45 km) have been used. For paths crossing a comparable amount of sea and land, a water layer (2 or 4 km thick for waves travelling through the Mediterranean region or the Atlantic Ocean respectively) has been introduced in the above-mentioned models. Starting from these models, we invert for *S* velocity and Moho depth. Moreover, crustal thickness at the earthquake source is accounted for by using the Moho map of Meissner *et al.* (1987) when excitation factors are computed. In addition to *a priori* information on the path average structure, a second criterion for the selection of the 1-D background models was the similarity between recorded and synthetic waveforms. Using surface wave ray theory (WKBJ approximation), the synthetic waveform depends on the average wavenumber along the path. Perturbations to the wavenumber are related to variations in the starting model using Fréchet derivatives (Takeuchi & Saito 1972), which are used to compute waveform derivatives.

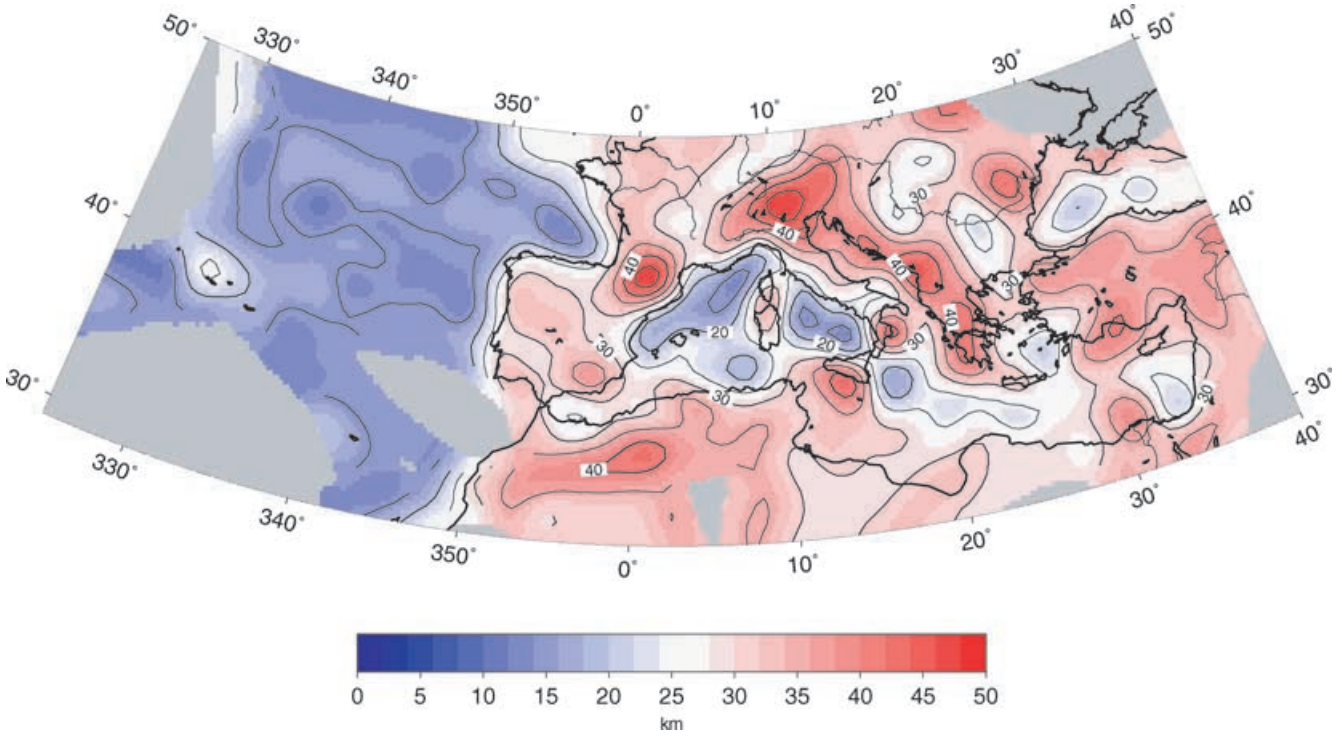

Figure 2. Obtained map for the depth to the Moho discontinuity (EAM02) discussed in detail in Marone *et al.* (2003).

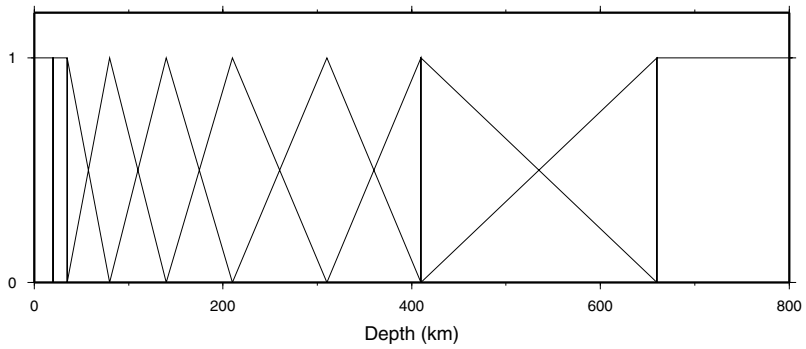

Figure 3. Set of basis functions used to parametrize the average velocity perturbation along the path between source and receiver. The deepest basis function describes a half-space. The depth to the Moho has been parametrized as well.

The average velocity perturbation along the path between source and receiver is parametrized in terms of a number of basis functions, which are a mix of boxcar and triangular functions in order to incorporate both discontinuities and gradients in the model (Fig. 3). The perturbations are then expressed in the form of linear equations with uncorrelated uncertainties (Nolet 1990).

The fits are dominated by phase matches for the waves of different modes and frequencies, while the amplitude differences between observed and synthetic waveforms are not explicitly included as constraints on Earth structure because of the strong ambiguity in the interpretation of Rayleigh wave amplitude anomalies (Van der Lee 1998). Since in PWI the observed and synthetic waveforms are compared in the time domain, it is possible to visually assess the amount and timing of contamination by scattering. We restrict the time window to waveforms that probably represent direct waves.

2.2 Point constraints on crustal thickness

To reduce trade-offs between Moho depth and velocity structure around it, which are inherent in the Rayleigh waves used in this study, we have collected independent estimates of Moho depth obtained from receiver function analysis, seismic refraction/reflection surveys and gravity data studies (see appendix A in Marone *et al.* (2003) for a complete list of references). Uncertainties related to the individual point measurements differ depending on the method used to determine the crustal thickness estimate. Under the assumption of a flat Moho (e.g. Van der Meijde *et al.* 2003), crustal thickness data obtained with receiver function analysis have an error around $\pm$1–2 km. Uncertainties related to the results of refraction and/or reflection seismology vary depending on the data quality. In general, results of gravity studies have larger errors.

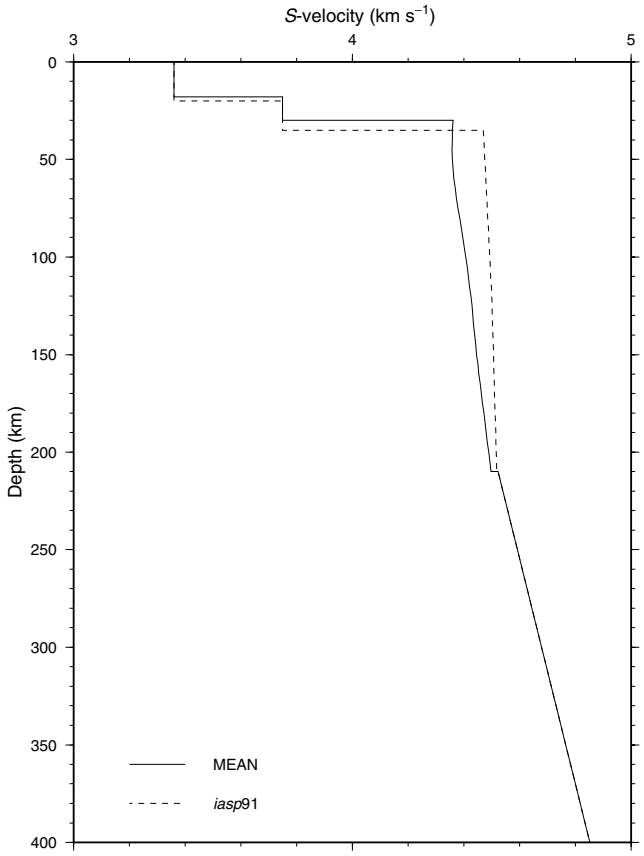

Figure 4. 1-D *S*-velocity model (MEAN) used as starting model in the 3-D inversion compared with iasp91 (Kennett & Engdahl 1991).

2.3 3-D inversion

The 3-D *S*-velocity model is parametrized as coefficients of a Cartesian grid of nodes, while for the Moho depth a triangular grid of nodes is adopted on a spherical shell (Van der Lee & Nolet 1997). For the *S*-velocity model, the distance between the nodes in the x and y directions is 100 km, and in the z direction 60 km. The Earth's surface is contained within the grid. The distance between the nodes of the triangular grid is compatible with the interknot spacing in the Cartesian grid and is 97 km on average. Trilinear interpolation was used to determine the value of the solution at a given point.

Since the 1-D path average velocity models obtained by fitting waves travelling through the Mediterranean region show that the crust is on average thinner than the 35 km of iasp91 and that the upper 200 km of the mantle are characterized by low velocities, we have used a reference model in the inversion for the 3-D *S*-velocity structure that is similar to iasp91, but has a crustal thickness of 30 km and lower *S* velocities in the upper mantle (Fig. 4). However, the obtained 3-D solution is robust and does not depend on the adopted 1-D starting model: minor differences, smaller than the expected standard deviation, are observed for the amplitudes of the anomalies, while the shape and position of the velocity anomalies are robust features. A similar solution is also obtained using as starting model the 3-D *S*-velocity model shown later in Fig. 11.

Since the algorithm used to solve the system of equations (LSQR Paige & Saunders 1982) yields a minimum-norm solution, we work with a dimensionless model vector. The model vector is made dimensionless by scaling it with the expected standard deviation of the model parameters: 225 m s^{-1} for *S* velocities and 4 km for Moho depths. Since we are jointly inverting two different sets of constraints, the system has to be scaled. The data covariance matrix $\mathbf{C}_\mathrm{d}$ scales each row of the constraint matrix, controlling the relative importance of each constraint. As scaling factor, the estimated uncertainty of each constraint is used: for surface wave constraints derived in the waveform fitting procedure based on the eigenvalues of the Hessian matrix (Van der Lee & Nolet 1997) and for point constraints taken from the literature (see Section 2.2).

We obtain the linear system of equations:

$$\mathbf{C}_\mathrm{d}^{-1/2}\mathbf{A}\mathbf{m} = \mathbf{C}_\mathrm{d}^{-1/2}\mathbf{d} \tag{2}$$

where $\mathbf{A}$ is the constraint matrix, $\mathbf{m}$ the model and $\mathbf{d}$ the data vector. To imitate the wide sensitivity region of long-period waves, we require *a priori* that the velocity in the Mediterranean region varies smoothly. Smoothing was applied horizontally. The value of the smoothing function decreases linearly from the centre to zero at a chosen distance. This means that we express the model $\mathbf{m}$ as:

$$\mathbf{m} = \mathbf{S}\mathbf{n} \tag{3}$$

where $\mathbf{S}$ is the smoothing matrix and $\mathbf{n}$ the rough model. The system becomes:

$$\mathbf{C}_\mathrm{d}^{-1/2}\mathbf{A}\mathbf{S}\mathbf{n} = \mathbf{C}_\mathrm{d}^{-1/2}\mathbf{d} \tag{4}$$

which is rewritten as:

$$\mathbf{H}\mathbf{n} = \mathbf{q} \tag{5}$$

where $\mathbf{H} = \mathbf{C}_\mathrm{d}^{-1/2}\,\mathbf{A}\mathbf{S}$ and $\mathbf{q} = \mathbf{C}_\mathrm{d}^{-1/2}\,\mathbf{d}$.

We add regularization equations to the system that bias the rough solution $\mathbf{n}$ towards zero norm. The system then becomes:

$$\begin{pmatrix}\mathbf{H}\\ \lambda\mathbf{I}\end{pmatrix}\mathbf{n} = \begin{pmatrix}\mathbf{q}\\ \mathbf{0}\end{pmatrix} \tag{6}$$

where λ is the damping coefficient. We solved this linear system of equations iteratively using the least-squares algorithm LSQR (Paige & Saunders 1982).

3 DATA

The coverage of the Mediterranean region with broad-band seismic stations is inhomogeneous. While for Europe the availability of broad-band data in the last decade has significantly increased, broad-band stations are non-existent or rare in northern African countries, on Mediterranean islands and on the seafloor. Moreover, because the Mediterranean upper mantle is characterized by strong lateral heterogeneities associated with subduction of the African Plate, which results in distortion of the waveforms by scattered energy, we need to include relatively short wave paths. For these reasons, during the MIDSEA project, 25 broad-band recording instruments were temporarily installed in locations with a poor station density (Table 1) (Van der Lee *et al.* 2001). In addition to data of the temporary MIDSEA network, seismograms recorded by permanent broad-band stations of the Swiss National Network (Baer 1990), IRIS, MedNet (Boschi *et al.* 1991), University of Trieste, Géoscope (Romanowicz *et al.* 1984), RéNaSS, TGRS, GEOFON (Hanka & Kind 1994), GRSN (Hanka 1990), GRF, University of Stuttgart, GII, University of Barcelona, University of Madrid, Institute Andaluz, Czech National Seismological Network (CZ), NARS (Paulssen 1992), GI_Budapest and Blacknest have been collected (Fig. 5).

For this study we selected vertical and radial component seismograms with a good signal-to-noise ratio for *SV* and/or Rayleigh

Table 1. Location of the MIDSEA stations.

Code	Location	Latitude	Longitude	Altitude (m)
CDLV	Spain	29.163	−13.444	37
EBRE	Spain	40.823	0.494	36
MELI	Spain	35.290	−2.939	40
POBL	Spain	41.379	1.085	550
DUOK	Croatia	44.113	14.932	115
HVAR	Croatia	43.178	16.449	250
APER	Greece	35.550	27.174	250
ITHO	Greece	37.179	21.925	400
KOUM	Greece	37.704	26.838	340
GHAR	Libya	32.122	13.089	650
MARJ	Libya	32.523	20.878	650
CALT	Italy	37.579	13.216	955
DGI	Italy	40.318	9.607	343
GRI	Italy	38.822	16.420	525
MGR	Italy	40.138	15.553	297
SOI	Italy	38.073	16.055	300
VENT	Italy	40.795	13.422	110
ABSA	Algeria	36.277	7.473	1025
RUSF	France	43.943	5.486	520
SMPL	France	42.094	9.285	405
COV2	Portugal	39.677	−31.113	194
PGRA	Portugal	39.029	−27.981	245
PSCM	Portugal	38.701	−27.117	400
PSJO	Portugal	38.422	−28.303	258
PSMA	Portugal	36.996	−25.131	249

waves for regional events occurring between 1985 and 2002 (Fig. 5). Our data set consists of events with a magnitude between 4.1 and 7.6. The hypocentre depth ranges from 1.5 down to 396 km. The epicentral distance is, except for the events located in the Atlantic Ocean, $<30^\circ$ and the median path length is 15°. For the synthetic seismogram calculation the hypocentre location and origin time were taken from NEIC preliminary determination of hypocentres for recent earthquakes, from the catalogue of Engdahl *et al.* (1998) and from Engdahl (personal communication) for older events, and the moment tensor solutions from online Harvard catalogues (e.g. Dziewonski *et al.* 1994) when available. For small regional events that occurred between 1999 and 2002 we used the solutions computed by Braunmiller *et al.* (2002). In a few cases we adopted the focal mechanisms from the online MedNet catalogue (http://www.ingv.it/seismoglo/RCMT/) or obtained by Thio *et al.* (1999). Only azimuths away from the fundamental mode Rayleigh wave source-radiation nodes have been considered.

For each selected seismogram, after a quality check and deconvolution of the instrument response, one or two time windows containing the fundamental and/or higher modes of the Rayleigh waveforms were interactively fitted. Selection of two distinct windows for the fundamental and higher modes allows relative weighting of the different wavepackets, enhancing the contribution of the low-amplitude, short-duration higher modes with respect to the dominating fundamental mode. Moreover, different and more appropriate frequency ranges for body and surface waves can be used, in the optimal case down to as low as 6 mHz for the fundamental mode and up to 100 mHz for short paths. After data selection and following analysis, 1136 fitted waveforms of vertical and radial component seismograms from 235 events recorded by 117 different seismic stations have been obtained (Fig. 5), which result in 8212 linear constraints on the 3-D upper-mantle *S*-velocity structure for the Mediterranean region.

4 PREFERRED MODEL

Solution of underdetermined problems is non-unique and a set of models exists which fit the data equally well. Models differ depending on the regularization applied, on the cell size and on the smoothing parameter chosen for the inversion. In Fig. 6, two end-members of the possible solution range are shown. The quality of the fit to the data of the *a posteriori* synthetics computed with these two models is comparable. For the first *S*-velocity model presented, a node

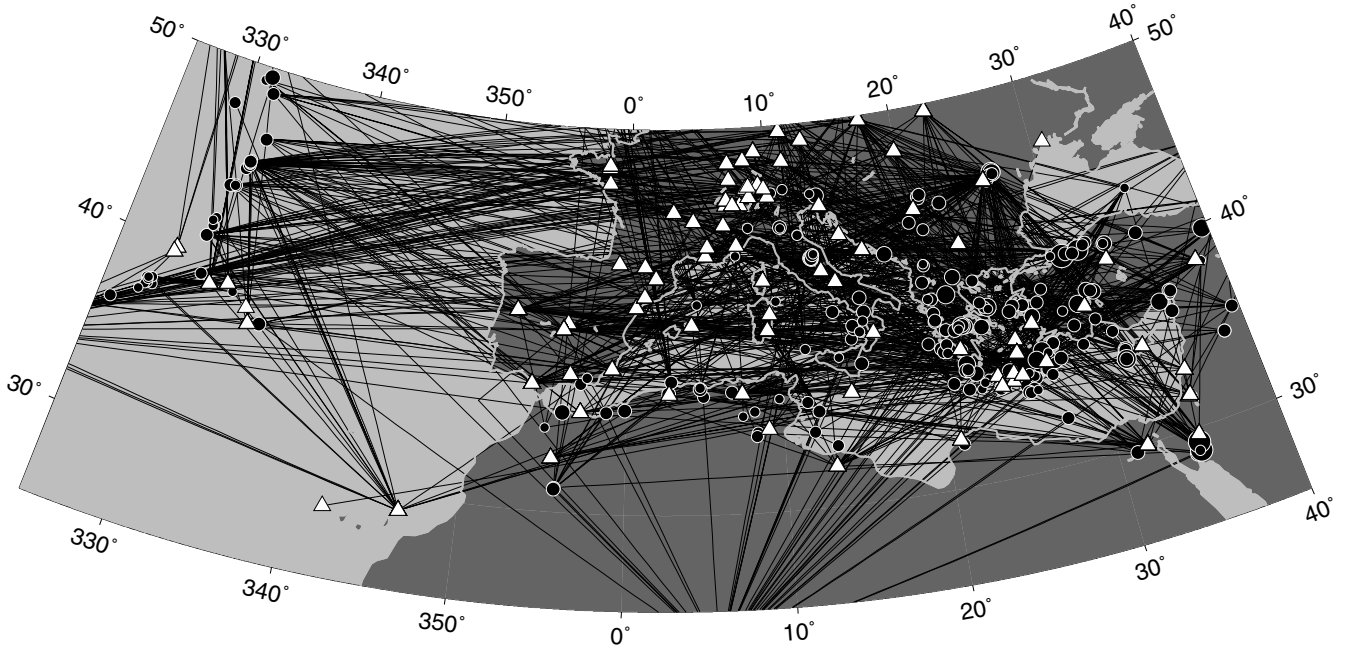

Figure 5. Great circle ray paths for the 1136 seismograms used in this study. White triangles and black dots represent used broad-band seismic stations and events, respectively.

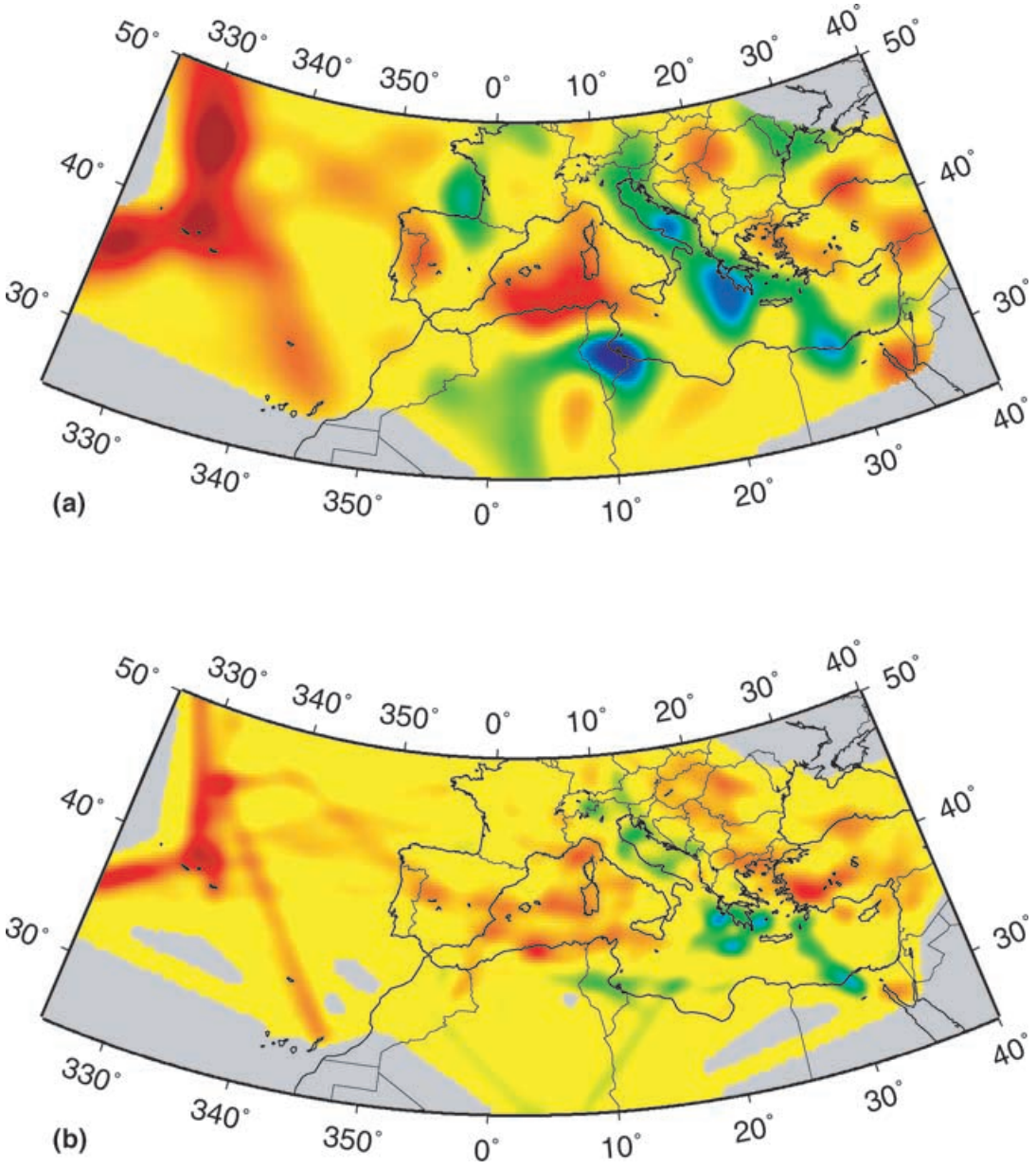

Figure 6. Horizontal slices at 100 km depth through two *S*-velocity models, which show a comparable fit to the data: (a) 'smooth' model obtained with a node spacing of 100 km and 60 km in the horizontal and vertical directions respectively, and a smoothing function half-width of 300 km; (b) 'rough' model obtained with a smaller grid spacing (50 km and 30 km in the horizontal and vertical directions) and a smaller half-width for the smoothing function (100 km).

spacing of 100 km and 60 km in the horizontal and vertical directions respectively and a smoothing function half-width of 300 km have been chosen. The characteristic wavelength of the anomalies in this model is comparable with the size of the features imaged, for example in regional tomographic results obtained from global measurements (Boschi 2001). The second example has been chosen because it shows the same characteristics, in terms of model roughness and anomaly size, as *P*-velocity models (e.g Piromallo & Morelli 2003). This solution has been obtained using a finer Cartesian grid of nodes (50 km and 30 km in the horizontal and vertical directions) and a smaller half-width for the smoothing function (100 km) compared with the previous example. However, the reliability of this model is questionable because of artefacts introduced by the increased relative influence of noise and wave-path distribution.

An estimate of the details which can be resolved with the data set used guides the selection of node spacing and smoothing parameter. First, the resolving power of a seismogram for the average Earth structure along its path is controlled by the Fresnel zone. If ray theory is used, as in this study, heterogeneities smaller than the width of the first Fresnel zone cannot be resolved. To exceed this limit, scattering of surface waves should be taken into account as described by, for example, Meier *et al.* (1997), Marquering *et al.* (1998) and Friederich (2003). Second, due to the averaging properties of surface waves propagating along a great circle, better resolution is expected in depth than in the horizontal directions (Figs 7 and 8). For these reasons, we chose the node spacing in the z direction to be 60 km, smaller than the 100 km node spacing selected for the x and y directions. The lesser resolution in the horizontal directions is

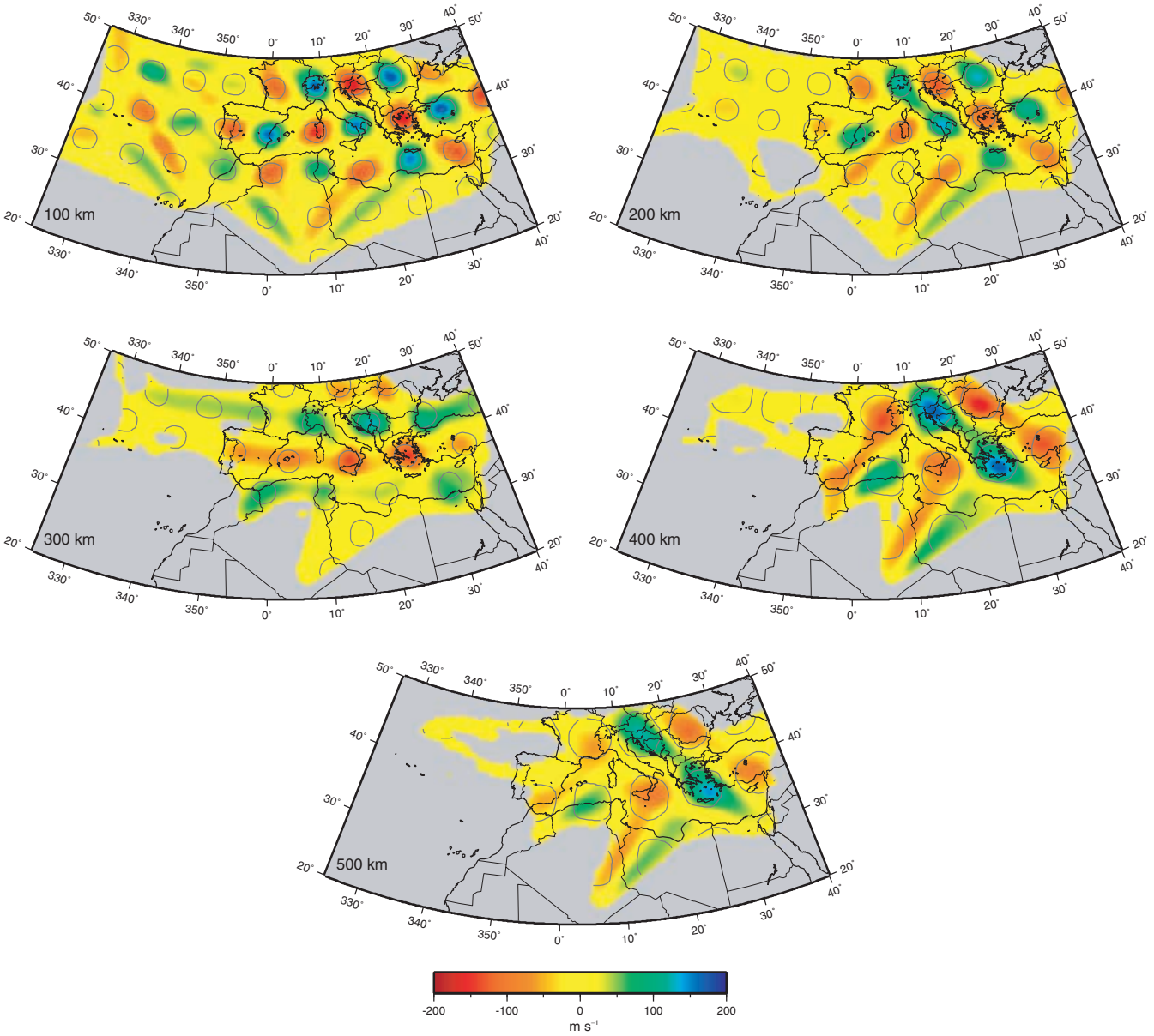

Figure 7. Spike resolution test results at different depths. The input model is represented by the grey contours at ± 100 m s^{-1}. The anomalies of the output model are shaded.

additionally taken into account by a smoothing function, which in the preferred model has a half-width of 200 km.

The value of the damping parameter λ was chosen so as to optimize the trade-off between variance reduction and model size and was set equal to 1.0. Damping is responsible for the strong underestimation (up to 60–70 per cent) of the amplitude anomaly in the lower upper-mantle (400–600 km).

The possible contamination of the sub-Moho mantle velocity structure arising from trade-offs with the insufficiently controlled crustal *S* velocities has been investigated in an inversion with fixed crustal structure (CRUST2.0 of Bassin *et al.* 2000). In regions with an anomalously low average crustal velocity due to thick sedimentary deposits (up to 14 km in the eastern Mediterranean) the uppermost mantle velocity (down to 80–90 km depth) could be underestimated by about 0.1 km s^{-1}.

The joint linear inversion of the constraints derived from the waveform fitting (see Section 3) and independent estimates of crustal thickness (Marone *et al.* 2003) according to the described parametrization and regularization yields our 3-D *S*-velocity model (EAV03). The inversion starting with MEAN (Fig. 4) resulted in a 96 per cent variance reduction and the remaining rms residuals were approximately three estimated standard deviations.

The fit to the data was assessed by calculating *a posteriori* synthetic waveforms and comparing them with the data. *A posteriori* synthetic seismograms have been computed by mode summation using 1-D averages through the obtained 3-D velocity model along the source–receiver paths (Fig. 9). The fit to the data is good both for the fundamental-mode Rayleigh wave trains and the higher-mode body wave trains. Owing to the applied damping and smoothing and to the least squares nature of the 3-D inversion, the 'posteriori' fits

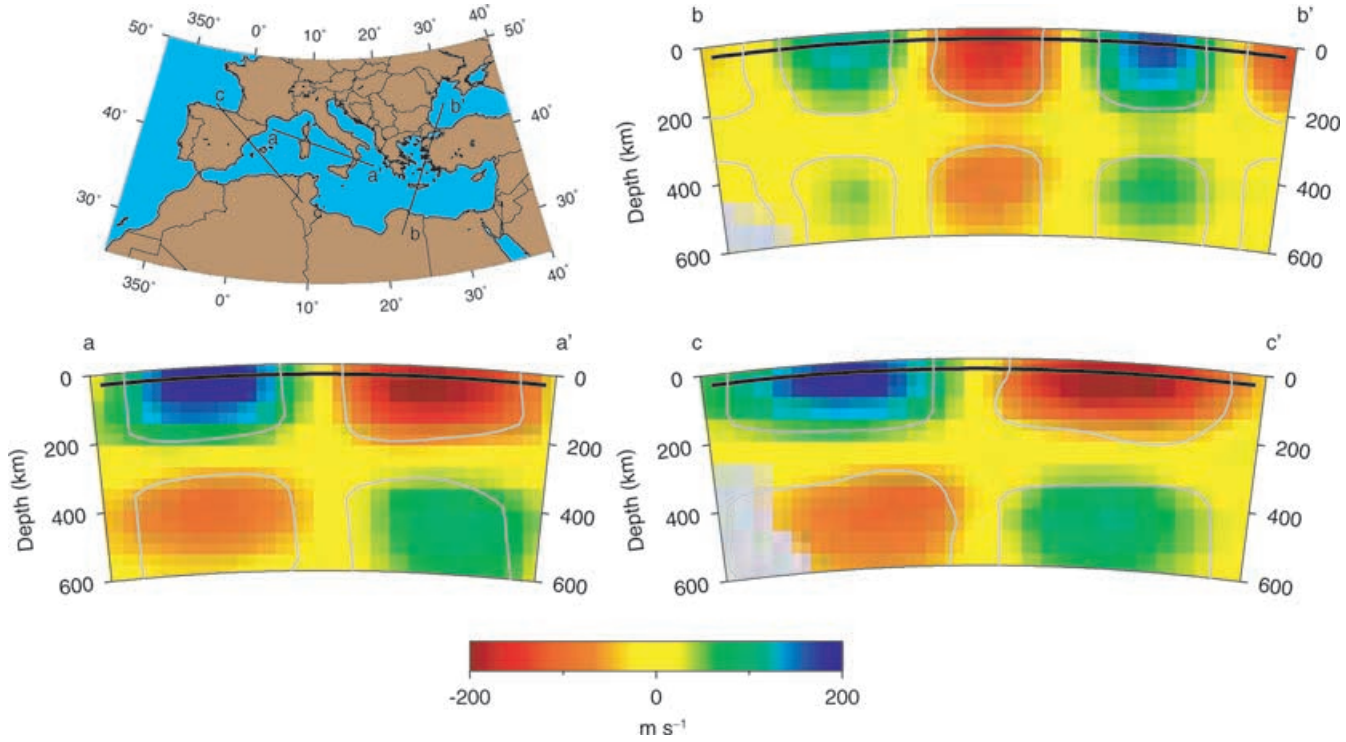

Figure 8. Spike resolution test results for three different cross-sections taken along the great circle segments shown in the map. The ± 150 m s^{-1} level of the anomaly amplitude of the input model is represented by the contours. The anomalies of the output model are shaded (the horizontal and vertical scales are the same).

are not as good as the individual 'final' fits (not shown here), and as expected the misfit distribution is slightly wider than for the 'final' fits (Fig. 10). However, a significant improvement compared with the 'initial' waveform fits (Fig. 9) is observed as well as a significantly narrower misfit distribution (Fig. 10). A systematic analysis of the ray paths with the worst 'posteriori' fits did not show any clear correlation with geography or epicentral distance.

5 RESOLUTION

The coverage of the Mediterranean region with great circle wave paths, from which linear constraints have been derived with the waveform fitting procedure, gives a first idea of the resolution which can be achieved with our data set. Fig. 5 shows that the path coverage is not homogeneous. For eastern and central Europe and the northern part of the Mediterranean Basin an optimal resolution can be expected, because the region is sampled by a large number of crossing waves. However, for the eastern Atlantic Ocean, for the southern Mediterranean Basin and especially for the northern Sahara, the path coverage is sparse due to an inconvenient distribution of stations and events. The path density is not as high as for continental Europe and for the northern Mediterranean Basin and most waves travel in parallel. Therefore the resolution will be limited and lateral smearing along the main path directions has to be expected.

To assess the resolving power of our data set we have performed tests, in which a known earth model and the data sensitivity matrix (**H** in eq. 5) of our system are used to compute synthetic data (**q** in eq. 5). After adding Gaussian distributed noise so as to simulate the same signal-to-noise ratio as for the data, the inversion is performed with the same parameters as for the real data. To test different aspects of the resolution, a series of different earth models has been chosen, ranging from a completely unrealistic but standard pattern of spike anomalies to realistic models simulating, for example, subduction zones and asthenospheric layers. A series of checkerboard tests with synthetic anomalies at different depths, of different sizes and arranged in different patterns shows that the resolution decreases with depth and bigger anomalies are better resolved than smaller ones. Also, the recovered anomaly amplitude decreases with depth. Horizontal smearing in the main path direction is observed in regions with insufficient crossing paths. This effect is more prominent at depth. Examples are shown in Figs 7 and 8. The input models for these resolution tests consist of variable-size *S*-velocity anomalies of alternating sign with an amplitude of ± 250 m s^{-1} and ± 400 m s^{-1} relative to MEAN (Fig. 4) in Figs 7 and 8 respectively. The best resolution is observed at depths of 75–100 km, where the anomaly shape is well recovered and the amplitude is restored up to 70 per cent for the Mediterranean region, eastern, central and western Europe. Beneath northern Africa, the Atlantic European coast and the eastern Atlantic Ocean the resolution is limited due to insufficient data, and horizontal smearing along the dominant wave path direction is observed. At a depth of 300 km, for the regions with the best path coverage, the anomalies are fairly well recovered, even if smearing in an east–west direction is present and the magnitude of the anomalies is underestimated by 50 per cent because of damping applied in the inversion. Thanks to the inclusion of constraints from higher-mode waveforms, the sensitivity deeper in the upper mantle is still significant. As deep as 500 km, 800-km-wide structures can still be detected beneath Europe and the Mediterranean region. However, up to 50 per cent of the original anomaly amplitude can be recovered only beneath the eastern and central part of the Mediterranean. For northern Africa and the western Mediterranean Basin no more than 25 per cent of the input amplitude is restored. Our

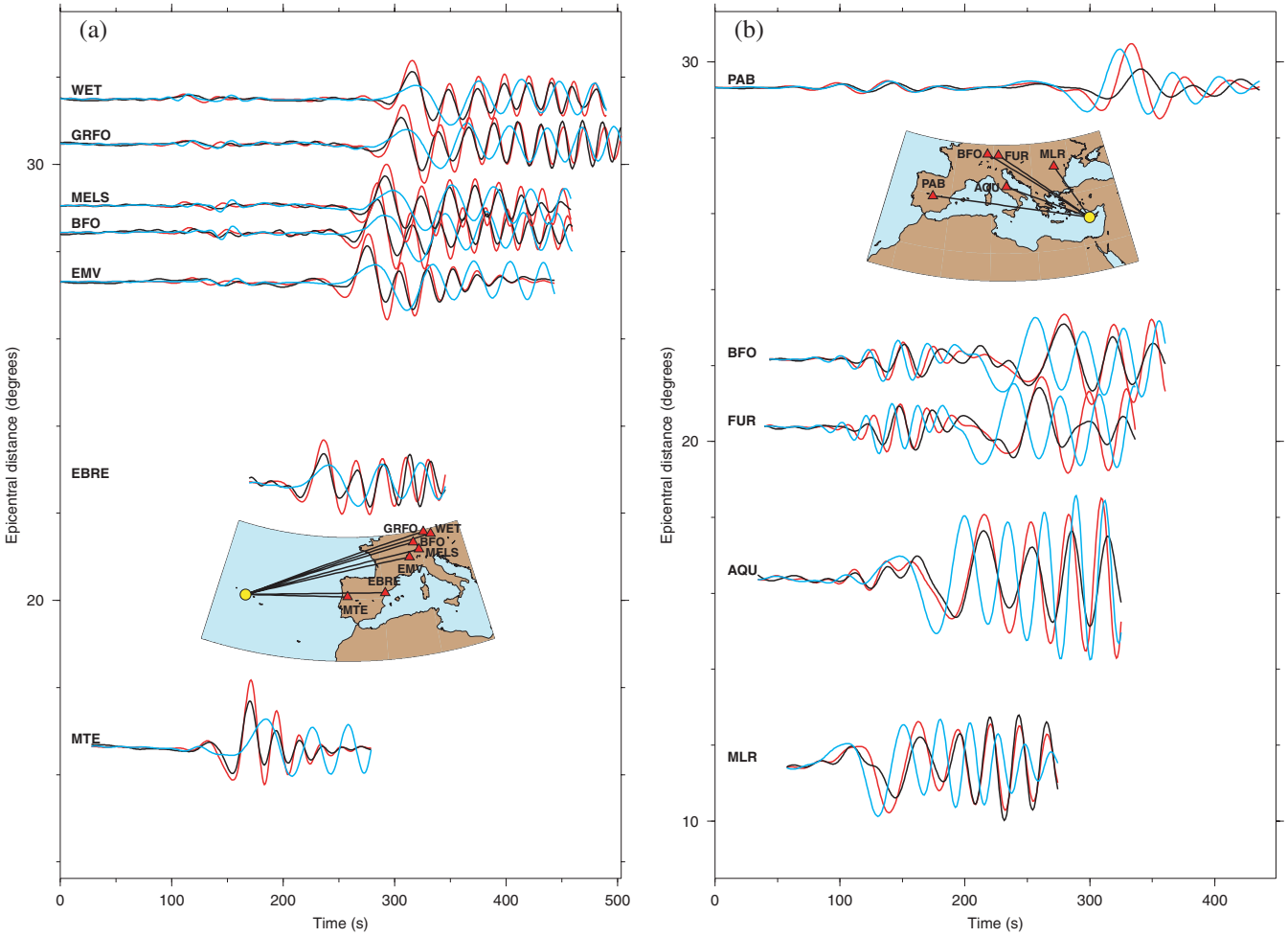

Figure 9. Observed waveforms (black lines), synthetic seismograms computed with MEAN (blue lines) (Fig. 4) and with EAV03 (red lines). The wave paths and the location of the events and stations are shown in the insets. A reduction velocity of 6 km s^{-1} has been used: (a) for the event on 2000 August 1 (M_w 5.1) at the mid-Atlantic ridge; (b) for the event on 1995 May 29 (M_w 5.3) on Cyprus.

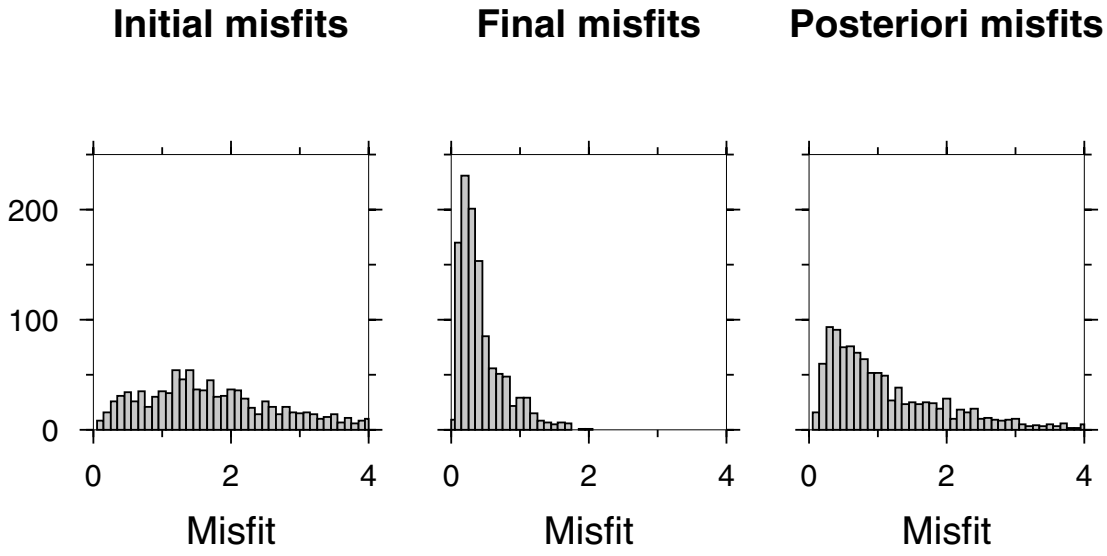

Figure 10. Histogram for the misfit for each waveform computed according to eq. (1). On the left, misfit of synthetics computed using MEAN ('initial' fits); in the centre, calculated with the best 1-D path-averaged model ('final' fits); on the right, calculated from EAV03 ('posteriori' fits). The total misfit reduction from 'initial' to 'final' is 81 per cent, and from 'initial' to 'posteriori' is 41 per cent.

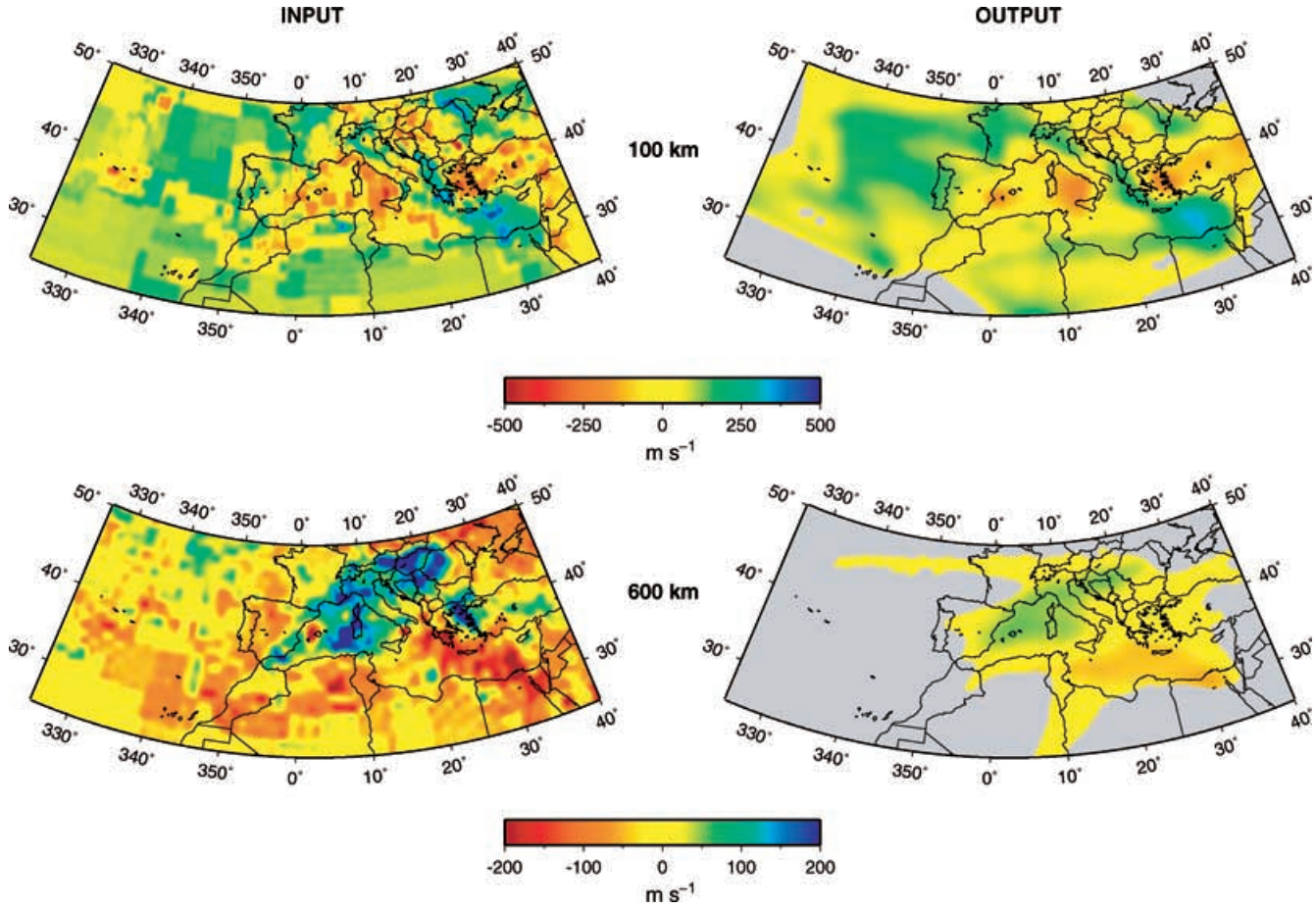

Figure 11. Results at two different depths of a recovery test with a realistic input model (on the left) simulating structures present in the Mediterranean region. The recovered model is shown on the right.

data set provides an excellent resolution of the depth extent of the anomalies as shown in Fig. 8.

The resolution was further investigated using a model with more realistic anomalies simulating subducting lithosphere beneath, for example, the Hellenic and the Calabrian arcs and an asthenospheric layer beneath, for example, the western Mediterranean (Fig. 11). For this test an adapted version of the *P*-velocity model BSE_NL of Bijwaard & Spakman (2000) was used as the input structure. The recovered model shows that the short-wavelength *P*-velocity structure could not be resolved because the limit of the resolving power of the surface waves in the frequency range we used was reached and because of the applied smoothing. However, especially at shallow depths (75–150 km), the long-to-intermediate wavelength character of the input structures has been resolved. Even narrow features such as the high-velocity anomaly beneath the Hellenic Arc can be imaged with our data set. Deeper in the upper mantle, the major structures could be imaged down to 600 km, although the anomaly amplitudes are reduced by 50 per cent and horizontal smearing is observed in regions with a poor crossing wave path coverage.

We carried out further testing to check that no structural bias is introduced by the wave-path geometry and data sensitivity. For this purpose we used a constant synthetic model, with a velocity anomaly of 300 m s^{-1} and no added noise. In a second step the influence of noise has been tested using the same input structure, but adding noise vectors with different standard deviations to the computed synthetic data. As expected, it has been observed that with increasing standard deviation of the noise vector the amplitude of the recovered perturbations with respect to the constant synthetic model also increases, but that increasing damping is limiting the bias of the results due to noise. For the damping value used in this study, the anomaly amplitudes of the recovered noise artefacts are only one-eighth of those in the obtained *S*-velocity model, so that Gaussian distributed noise is not significantly biasing the recovered structure. In Fig. 12 an example is shown where the standard deviation of the noise vector has been chosen so as to simulate the signal-to-noise ratio of the real data.

Several inversions with different subsets of the complete data set have also been performed to investigate the influence of specific paths on certain anomalies. In a first step, the subsets have been created randomly. The inversion results show that the recovered upper-mantle *S*-velocity structure discussed in Section 6 is robust and does not depend on single paths. In a second step, data belonging to specific events have been removed to check the reliability of individual structures. Also in this case it turned out that the observed features are robust and do not depend on one single event or path.

In theory, the obtained *S*-velocity model could be biased by the presence of azimuthal anisotropy. In regions with a dense coverage with criss-crossing paths, this possible effect is reduced because the azimuthal variations are averaged out at each point of the model. The influence of azimuthal anisotropy on our model has been estimated (Lloyd 2003) by constructing a vector **q** that describes the

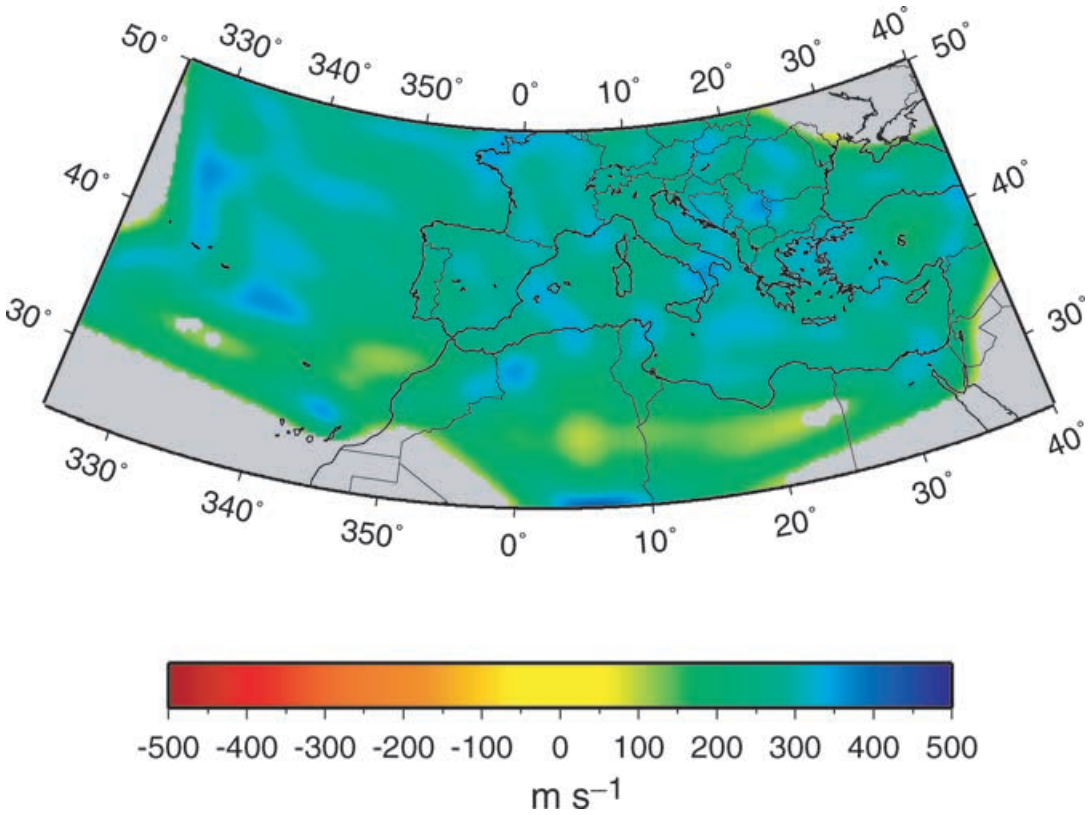

Figure 12. Results of a resolution test showing the effect of noise on the obtained velocity model at 100 km depth. The input model consists of a constant velocity anomaly of 300 m s^{-1}; the standard deviation of the noise vector has been chosen so as to simulate the signal-to-noise ratio of the data.

contribution of observed azimuthal anisotropy (Schmid *et al.* 2004) for each single path. The model obtained in an inversion using this **q** shows that the observed azimuthal anisotropy, even for the extreme case where it is concentrated in the thinnest possible shallow layer, is not significantly biasing our results. The strongest effect of ignoring the contribution of azimuthal anisotropy on our model is observed along the Italian peninsula, where large delay times between fast and slow wave components have been measured (Margheriti *et al.* 2003; Schmid *et al.* 2004). The effect is on a slab-like high-velocity anomaly elongated in the north–south direction, in that this anomaly appears less continuous in the north–south direction than in the case of taking azimuthal anisotropy into account.

6 RESULTS

The obtained *S*-velocity structure for the Mediterranean and surrounding regions (EAV03) is shown in horizontal slices at different depths in Fig. 13. The complex origin and evolution of this plate boundary area (Dercourt *et al.* 1986) is reflected in the structure of the upper mantle: the presented shear wave velocity model is strongly heterogeneous.

Compared with previous *P*-velocity (e.g. Piromallo & Morelli 2003) and *S*-velocity models (Zielhuis & Nolet 1994; Marquering & Snieder 1996) for the Mediterranean region, we extended the results for the Mediterranean Sea itself and for northern Africa. Also the crust and uppermost mantle structure beneath the eastern Atlantic Ocean is better constrained compared with existing *P*-velocity (e.g. Bijwaard & Spakman 2000) and *S*-velocity (e.g. Silveira & Stutzmann 2002) studies.

6.1 Mediterranean Sea

The Mediterranean Sea exhibits strong lateral variations in crustal (Marone *et al.* 2003) and upper-mantle structure (Fig. 13), confirming a different origin and evolution for the western and eastern parts.

The western Mediterranean Sea, in particular the Algero-Provençal Basin, is underlain by average to high velocities in the uppermost 80 km. Between 80 and 200 km *S* velocities as low as 4.2 km s^{-1} are the indication for an asthenospheric layer. Deeper, average *S* velocities for the Mediterranean region (4.6–4.8 km s^{-1}) are mapped. The lithosphere–asthenosphere system present beneath the Algero-Provençcal Basin can also clearly be seen in a 1-D average *S*-velocity profile (Fig. 14). A similar velocity profile is also observed for the Tyrrhenian Sea. However, higher velocities have been found below 100 km due to the presence of high-velocity subducted material beneath the Apennines and the Calabrian Arc.

Both the horizontal and the vertical extent of the imaged features are well resolved down to 300 km (Fig. 7). The low *S*-velocity layer between 80 and 200 km is also present in the results of Zielhuis & Nolet (1994), while *P*-velocity models (Spakman *et al.* 1993; Piromallo & Morelli 2003) show a more diffuse zone, in both the horizontal and vertical directions. This is probably due to different wave-path coverage and lower sensitivity of *P* waves to this structure.

The lithosphere–asthenosphere system of the western Mediterranean Basin clearly differentiates itself from the structure of the older (23–84 Ma) eastern Atlantic Ocean (Fig. 15) in that it has significantly lower *S* velocities down to 150 km as well as a thinner lithosphere (∼80 km) than in the Atlantic Ocean. Differences

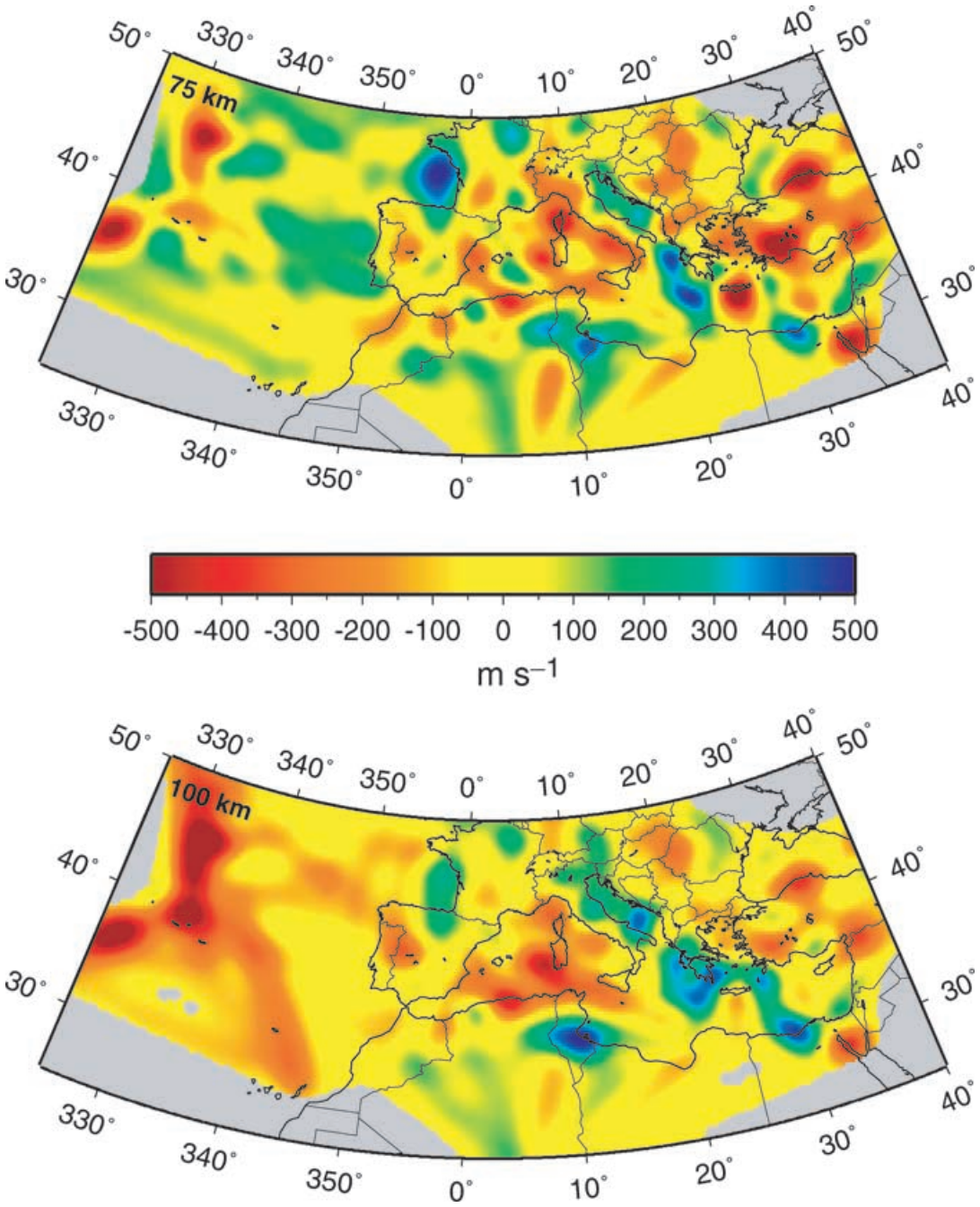

Figure 13. Horizontal slices at different depths through EAV03. Velocities are relative to MEAN (Fig. 4).

from the structure of a young ocean are also observed. Besides a narrower *S*-velocity minimum around 100 km depth and a smaller velocity gradient for the lithosphere, the western Mediterranean Basin also shows higher velocities (at least 0.1 km s^{-1}) between depths of 120 and 200 km than an oceanic structure of comparable age (Nishimura & Forsyth 1989). Its structure is also significantly different from the average velocity structure mapped at the mid-Atlantic ridge, where the imaged velocities are almost 0.2 km s^{-1} lower.

The imaged *S*-velocity structure beneath the western Mediterranean confirms that, rather than a young ocean, this basin could be a strongly stretched continent, partly affected by 'backarc' spreading, formed at the back of the northwestern subducting African oceanic lithospheric slab between ~30–22 Ma (Faccenna *et al.* 2001). The measured high heat flow (Burrus & Foucher 1986), the proposed reduced densities (Yegorova *et al.* 1998) and our low *S* velocities suggest that low viscosity material could be present at a shallow depth beneath the western Mediterranean.

The central Mediterranean, i.e. the area between southern Italy, Greece and Libya, is characterized by a sharp transition in *S*-velocity structure from north to south (Fig. 13). This is especially evident in the uppermost mantle (50–150 km), where *S* velocities as high as 4.8 km s^{-1} off the shore of Greece change abruptly to average *S* velocities for the Mediterranean Sea (4.4 km s^{-1}) along a line

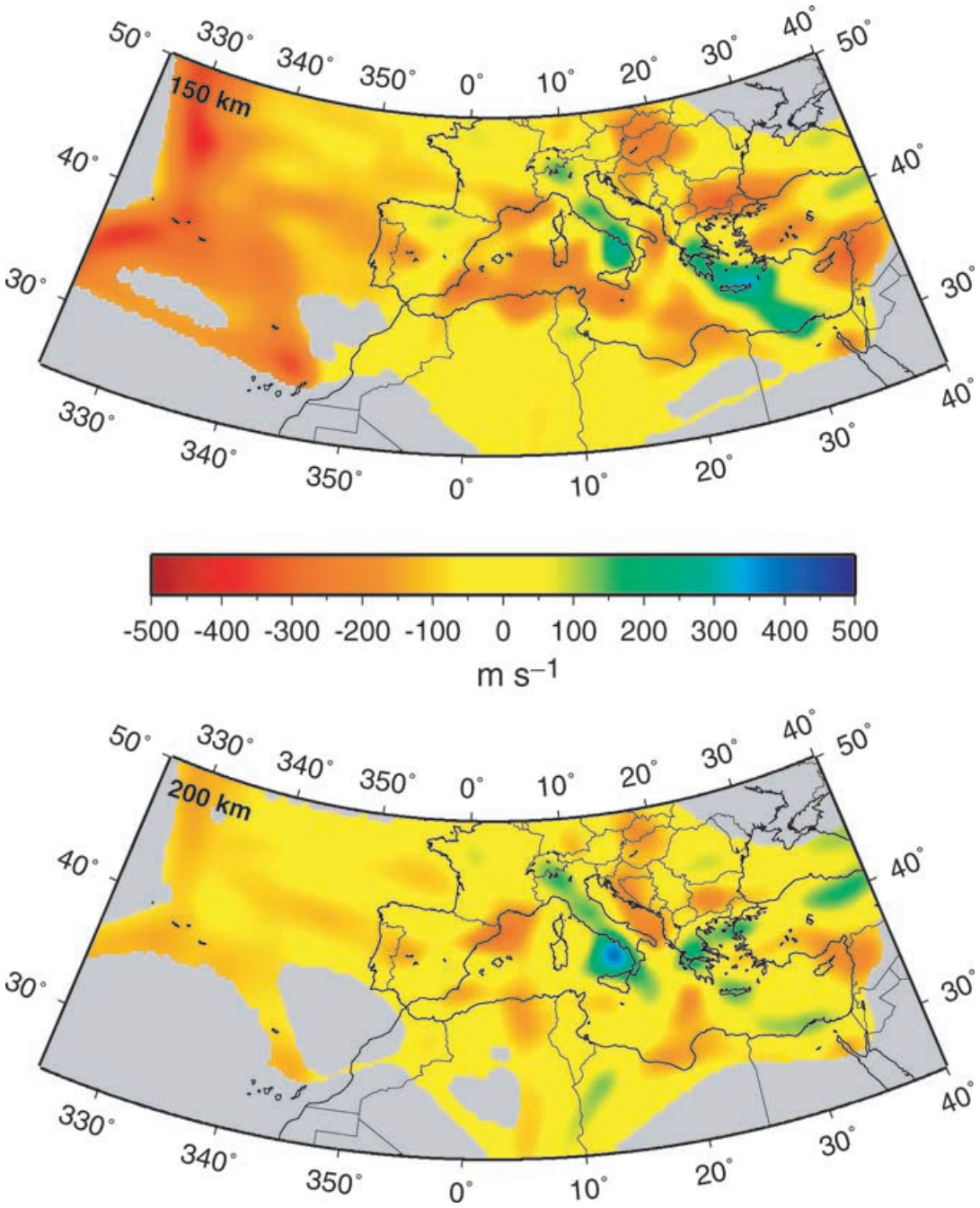

Figure 13. (*Continued.*)

connecting Sicily to Benghazi (Libya). At a depth of 200 km this abrupt velocity variation disappears and the entire region shows slightly low velocities (4.3 km s^{-1}).

The imaged and resolved (Fig. 7) structure correlates with the seafloor topography (Fig. 1). In fact, along the line connecting Sicily to eastern Libya an escarpment with a steep slope (the Malta escarpment) has been mapped at the surface of the sea bed. A similar feature has also been observed in the Moho topography (Fig. 2) (Marone *et al.* 2003). This transition in uppermost mantle *S* velocities, in crustal thickness and the escarpment at the surface could represent a suture zone between two blocks of different origin: deep oceanic basins (the Ionian and Sirte basins) to the north and a continental platform to the south (Dercourt *et al.* 1986).

The eastern Mediterranean is underlain by a completely different structure from the western part (Figs 13 and 14), implying a different origin and evolution of the two regions. The most striking difference is the absence, in the east, of a low-velocity layer between 100 and 200 km. On the contrary, average to high *S* velocities at these depths have been imaged. Between 150 and 200 km, low *S* velocities are mapped beneath Cyprus and the Turkey–Syria border region. No evidence of subducting or subducted material along the Cyprus Arc

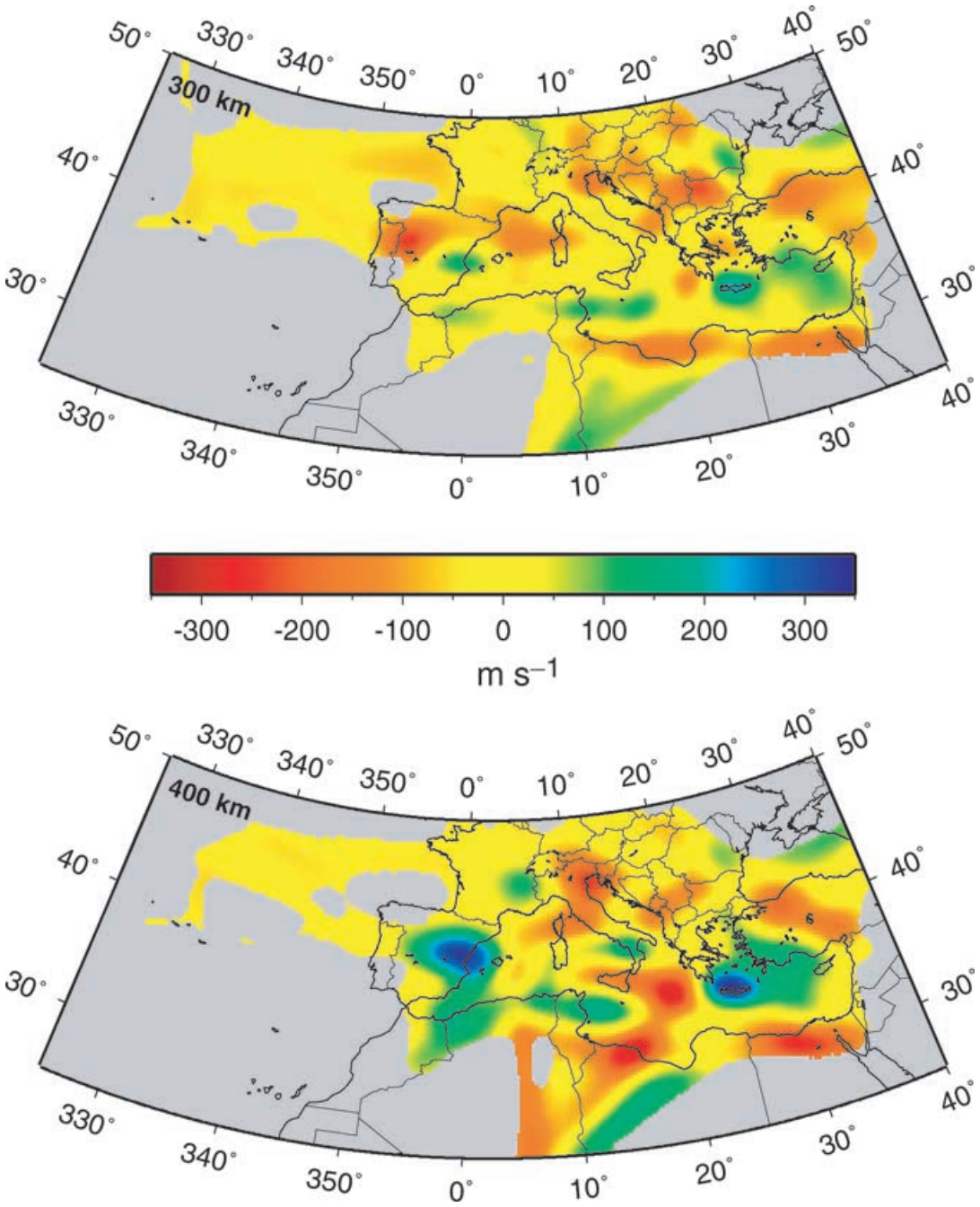

Figure 13. (*Continued.*)

is present. Synthetic tests (Fig. 7) show that the imaged structure is resolved down to at least 300 km.

The structure characterizing the eastern Mediterranean (missing asthenospheric layer and average iasp91 upper-mantle *S* velocities) suggests that this region is different from an oceanic basin or a strongly stretched continent. The imaged structure points to a continuation of the northern African continental lithosphere beneath the sea (Meier *et al.* 2003). However, our results do not rule out that oceanic microterranes could be alternated with originally continental domains. This small-scale heterogeneous structure would, however, be averaged out by the surface waves and imaged in our model as a rather homogeneous region having average iasp91 upper-mantle *S* velocities.

6.2 Northern Africa

In previous studies of the plate boundary in the Mediterranean region only few results have been given for the African side. Hardly any broad-band seismic stations had been installed along the northern African coasts, and due to the uneven event distribution in the southern Mediterranean the resulting path density was not high enough to achieve an acceptable resolution. The additional seismic stations

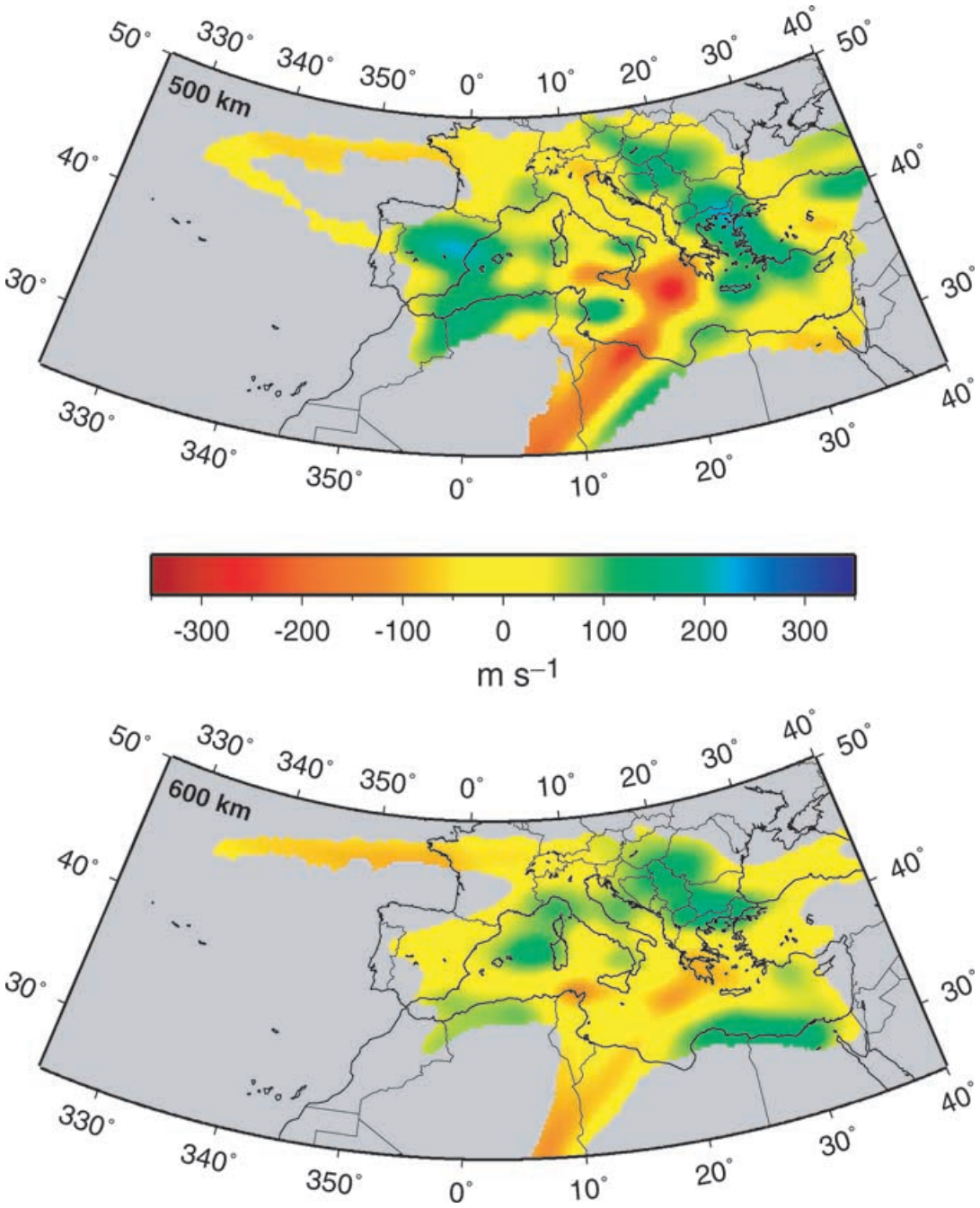

Figure 13. (*Continued.*)

installed in several northern African countries during the MIDSEA project (Van der Lee *et al.* 2001) are crucial to the resolving power we have achieved for this region.

EAV03 (Fig. 13) exhibits *S* velocities as low as 4.1 km s^{-1} for northern Algeria at a depth of 100 km. This negative anomaly, which is well resolved down to 200 km (Fig. 7), is an extension of the asthenospheric layer imaged beneath the western Mediterranean Sea. The deeper structure (beneath 300 km) is dominated by east–west striking high-velocity (4.7–4.8 km s^{-1}) features. Its north–south extent is well resolved, while the east–west trending could be affected by smearing (Fig. 7). Nevertheless, it can be concluded that, on average, the mantle at these depths is characterized by high shear wave velocities, possibly related to subduction processes which occurred in the area during the early Miocene (Dercourt *et al.* 1986).

Tunisia is characterized by *S* velocities higher than the average mean for the Mediterranean region at 100 km depth. This anomaly is reasonably well resolved, but the resolution rapidly decreases south of it, west of it and below (>150 km) it.

The resolution for the eastern part of the northern African margin is not as good as for the western part. Consequently, our model is close to the starting model of the 3-D inversion and does not show any significant feature in this region.

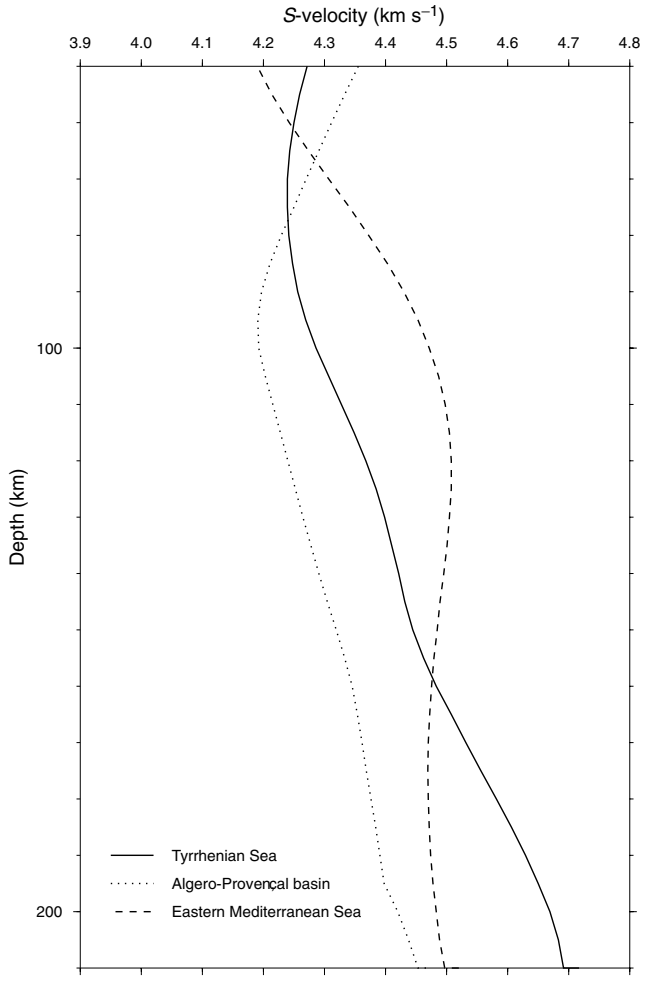

Figure 14. 1-D *S*-velocity models computed by averaging the velocity structure beneath the Algero-Provençal Basin, the Tyrrhenian Sea and the eastern Mediterranean Sea.

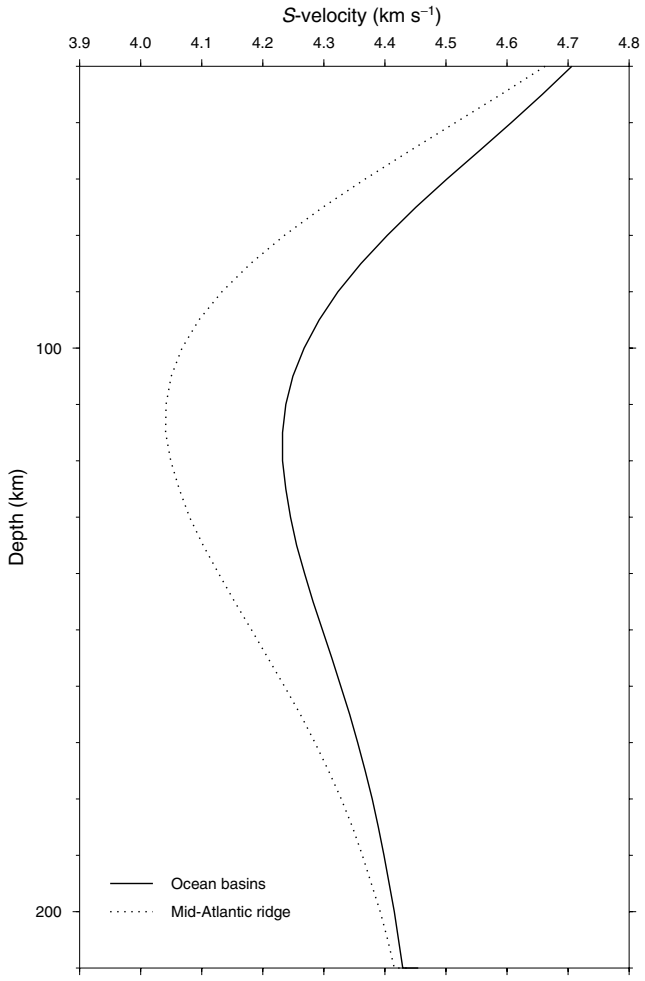

Figure 15. 1-D *S*-velocity models computed by averaging the velocity structure beneath the ocean basins and the mid-Atlantic ridge.

6.3 Eastern Atlantic Ocean

The plate boundary between the African and the Eurasian continents continues west of Gibraltar in the Atlantic Ocean as far as the Azores triple junction.

The imaged *S*-velocity structure for the eastern Atlantic Ocean (Fig. 13) is quite homogeneous, showing high velocities at a depth of 75 km between 25°W and the European coasts, while at the same depth a negative anomaly is mapped beneath the mid-Atlantic ridge and the Azores archipelago. This low-velocity feature is becoming more prominent at a depth of 100 km, while beneath the older oceanic basins average *S* velocities are observed. At 150 km the negative anomaly beneath the ridge and the Azores is still present. On average, slightly low velocities (4.3 km s^{-1}) at this depth are also imaged beneath the eastern Atlantic Ocean. Anomalously high velocities (up to 4.8 km s^{-1}) are imaged in the uppermost mantle beneath the Bay of Biscay. Isostatic studies (Marone *et al.* 2003) suggest lower densities for this region than expected at this depth for an old ocean; these workers related them to depleted lithosphere that had its origin in the Archaean.

Paths crossing the eastern Atlantic Ocean are generally longer than 20°. The path integral approximation used for the synthetics computation is satisfactory for the modelling of surface and body waves which bottom in the same depth range as the surface wave modes used. This condition is satisfied for both surface and body waves travelling for less than 2800 km, while this approximation is less accurate for larger epicentral distances because mode coupling is neglected (Marquering & Snieder 1996). Moreover, due to the shallow hypocentre depth of the earthquakes occurring at the mid-Atlantic ridge, the excitation of high-amplitude higher modes is limited. These factors restrict the use of higher modes for paths crossing the eastern Atlantic Ocean, thus reducing the imaging capability of our data set at depths greater than 200 km.

A similar image of the uppermost mantle in the eastern Atlantic has been obtained by Silveira & Stutzmann (2002) from Rayleigh and Love wave phase velocities.

Because of low spreading rates of the mid-Atlantic ridge (1 to 4 cm yr^{-1}), the age of the ocean floor rapidly increases with distance from the ridge axis. Owing to predominant west–east direction of the seismic waves travelling through the oceanic region (Fig. 5), the retrieved velocity structure is averaged out in this direction, hindering accurate observation concerning the dependence of the mantle velocity structure on lithospheric age.

6.4 Europe

The eastern continuation of the plate boundary can be followed beneath central, south and eastern Europe (Fig. 13). An almost continuous belt of high shear velocities (4.5–4.7 km s^{-1}) is imaged at a depth of 100 km beneath Italy, the Adriatic Sea, the Peloponnese and southern Greece. Deeper, these positive anomalies are limited to the Italian and Greek regions, while the former Yugoslavia is characterized by slightly low *S* velocities. High velocities are present continuously down to the transition zone only beneath Crete. This high-velocity belt dominating the central–eastern European upper mantle is interpreted as African oceanic lithosphere subducting beneath the European Plate, thereby marking the plate boundary.

Synthetic resolution tests show that the resolving power of our data set for central and eastern Europe is very good (Fig. 7). Beneath Italy and Greece, the regions with the highest path density, small-scale heterogeneities such as subducted lithosphere are imaged. In some regions, reduced sensitivity of the modelled waveforms for structures between 300 and 400 km prevents the imaging of continuous subducting slabs down to the transition zone, as, for example, beneath southern Italy.

Existing *S*-velocity models (Zielhuis & Nolet 1994; Marquering & Snieder 1996) also show the presence of high-velocity anomalies along the suture zone. However, lack of resolution hinders any conclusion about slab geometry and continuity. The general features imaged in *P*-velocity studies (Spakman *et al.* 1993; Wortel & Spakman 2000; Piromallo & Morelli 2003) compare well with EAV03, even though the *P*-velocity anomalies are narrower due to different data and imaging characteristics.

In more detail, EAV03 for Italy shows a continuous high-velocity anomaly from northern to southern Italy down to 300 km, interpreted as subducted lithosphere. Although synthetic tests indicate that both horizontal and vertical tears in the subducted body would be resolved by our data set, small gaps in the lateral continuity of the slab cannot be excluded.

A high-velocity body (4.7 km s^{-1}) has also been imaged beneath the Calabrian Arc between depths of 100 and 300 km (Fig. 16(a)). In the transition zone beneath the Tyrrhenian and Provençal basins, an indication of seismically fast material is also present. The small deviations of the imaged velocity from MEAN ($<$100 m s^{-1}) are a result of the strong underestimation of the anomaly amplitudes at these depths (see Section 5). These features have been interpreted as the image of subducted Ionian lithosphere. The thinness of this slab is close to the limits of the resolving power of our data set. Therefore we resolve such a structure only partly and it may be significantly smeared horizontally.

The high-velocity anomaly imaged in the Hellenic region extends from northern Greece, along the Hellenic Arc, all the way to the Turkish coast. This structure has been interpreted as subducted lithosphere. Further to the east no indications of subducted material are present.

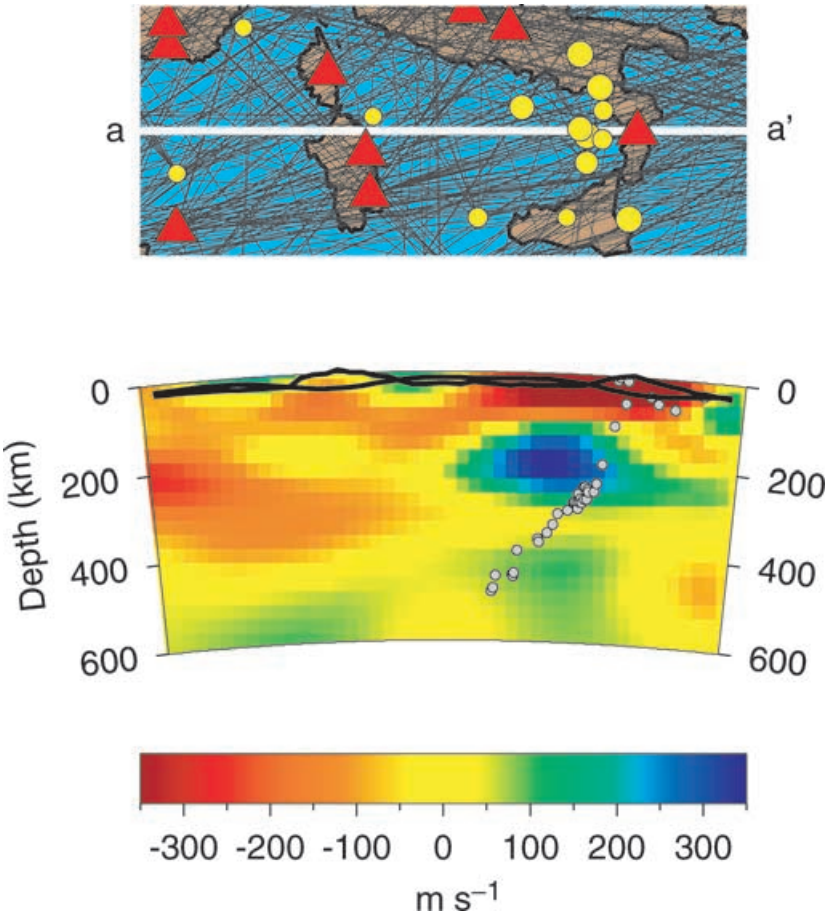

Figure 16. Vertical cross-sections through EAV03 along the great circle segments shown in the map in Fig. 8 (a saturated colour scale has been used to enhance structures in the transition zone; for the absolute values compare with Fig. 13 (the horizontal and vertical scales are the same)): (a) profile perpendicular to the Calabrian Arc; (b) profile from northern Libya to the Black Sea; (c) profile from northern Spain to northern Algeria.

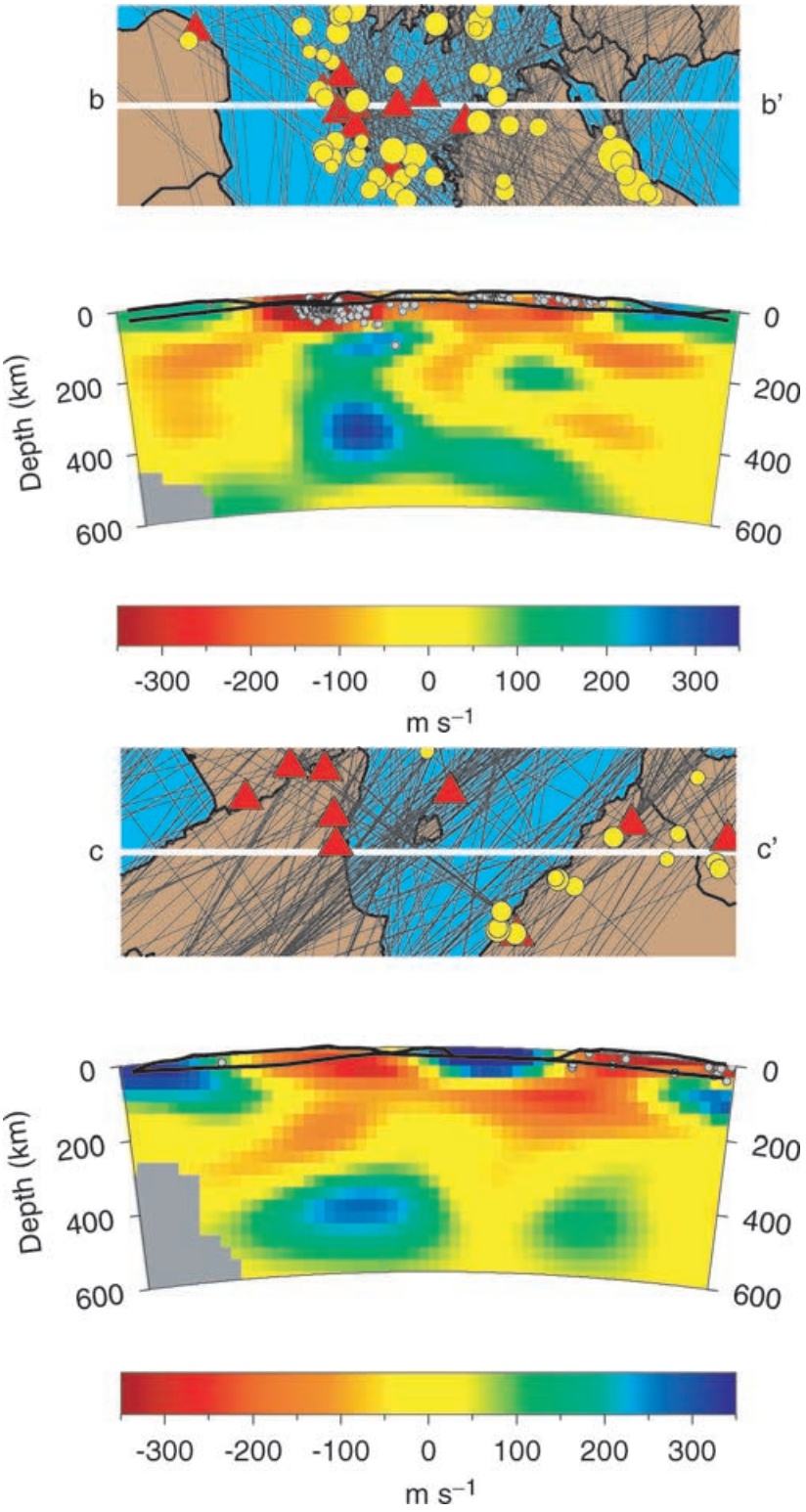

Figure 16. *(Continued.)*

Beneath Crete, we imaged a continuous steep positive anomaly, but with variable amplitudes, from 100 km depth down to the transition zone (Fig. 16b). At a depth of 500 km the slab is lying horizontally. Resolution tests show that the horizontal orientation of the imaged high-velocity layer is resolved and is not an artefact due to horizontal smearing.

Other relevant features present in our model are low *S* velocities between depths of 100 and 200 km beneath the Pannonian and the Moesian basins, regions dominated by extensional tectonics. Between depths of 75 and 100 km a negative cylindrical anomaly is also found beneath the Massif Central, which we interpret as hot mantle material close to the surface. This is in agreement with the

measured high heat flow (up to 110 mW m^{-2}) (Cermák & Rybach 1979) and with *P*-velocity models (Sobolev *et al.* 1997).

6.5 Iberian Peninsula

In this study we included additional data from MIDSEA stations and mid-Atlantic ridge earthquakes covering the Iberian Peninsula (Fig. 5), so that the resolution for Spain has significantly increased (Fig. 7). Beneath the western part of the peninsula, we imaged (Fig. 13) low *S* velocities (4.2 km s^{-1}) between 75 and 300 km, while the eastern Iberian margin below 250 km is characterized by a strong positive anomaly (this high-velocity feature is discussed further in Section 7.2).

7 DISCUSSION

7.1 Spreading ridges and old basins

Major structural differences in the eastern Atlantic Ocean are observed between the mid-Atlantic ridge and the older oceanic basins (see Section 6.3 and Fig. 13). In Fig. 15, 1-D average *S*-velocity models for these two regions are shown. The mean velocity structure for the deep basins is characterized by a fast 80-km-thick lithosphere, while a low-velocity layer (4.3 km s^{-1}) is present between depths of 90 and 130 km. The mean structure beneath the mid-Atlantic ridge is on average 0.2 km s^{-1} slower down to a depth of 120 km. Our results confirm that the North Atlantic lithosphere is characterized by lower velocities beneath the spreading ridge than under the old ocean basins as observed in regional 3-D models obtained using surface wave phase velocities (e.g. Mocquet & Romanowicz 1990; Silveira & Stutzmann 2002) or *S*-wave traveltimes (e.g. Grand 1994). Comparison of the average 1-D uppermantle structures with results for the Pacific Ocean obtained by Nishimura & Forsyth (1989), for example, shows that on average the eastern Atlantic Ocean is characterized by higher *S* velocities down to a depth of 150 km than areas of a similar age. Despite strong differences observed in the crustal structure between the mid-Atlantic ridge and the Azores (Marone *et al.* 2003), EAV03 does not reveal significant differences in the upper-mantle *S*-velocity structure. However, due to the limited resolution of our data set in this region, we cannot exclude that the mid-Atlantic ridge and the Azores distinguish themselves not only in their crustal but also in their uppermantle structure. With the current extension of the MIDSEA broadband network towards the west (Van der Lee *et al.* 2001; Silveira *et al.* 2002), the availability of high-quality data for the westernmost part of the Eurasia–Africa plate boundary has significantly increased, giving the opportunity to obtain a better-constrained model for this region.

7.2 Slab fragments in the western Mediterranean

EAV03 adds new information for a better understanding of the evolution of the western Mediterranean. In particular, we have mapped a high-velocity anomaly beneath eastern Spain between a depth of 250 and 500 km which could be related to the early stage of subduction in the western Mediterranean (Fig. 16c). Although resolution tests show that the shape of this feature is affected by smearing, the existence of the heterogeneity is resolved.

The strongest high-velocity heterogeneity imaged in *P*-velocity models (e.g. Blanco & Spakman 1993) beneath Spain is located further south than in our model, beneath the Alboran Sea and the Betic Cordillera. West of the Balearic Islands a significant positive anomaly, although limited in size, is visible only around 500 km.

Processes involved in the evolution of the eastern Iberian Peninsula are still a matter of debate and different tectonic reconstructions of the western Mediterranean are in disagreement (Carminati *et al.* 1998; Zeck 1999; Faccenna *et al.* 2001).

Northwest subduction of oceanic lithosphere along the eastern Spanish coast began about 80 Ma as consequence of the continuous Africa–Eurasia convergence (Dercourt *et al.* 1986). The first evidence of trench migration and backarc extension dates back to 30 Ma (Faccenna *et al.* 2001). We suggest that the deep imaged high-velocity body west of the Balearic Islands could be a fragment of this subducting slab, which detached before trench migration started (at 30 Ma). For instance, as suggested by Zeck (1999), the slab could have been segmented in three distinct arcs separated by transform faults. A lithospheric fragment from one of these segments could have sunk to the transition zone. This event could be at the origin of the unusual evolution of the Valencia Trough: rifting in this extensional basin began during late Oligocene–early Miocene and then suddenly failed around 18 Ma (Watts & Torné 1992). Although more investigation is needed to understand mechanisms and chronology, the new image of the eastern Iberian upper mantle could represent a useful element for the reconstruction of the history of the western Mediterranean.

7.3 Transition zone

Including body waves in our waveform fitting, which, however, do not bottom in the mantle beneath the realm of the surface wave modes, has provided sufficient resolution to image the gross-scale structure in the transition zone beneath the studied region (Fig. 7) and guards against the tendency for the sign of the heterogeneities to reverse with depth due to the neglect of surface wave mode coupling (Marquering & Snieder 1996). While the uppermost mantle of the Mediterranean is dominated by low-rigidity material, the picture changes dramatically in the transition zone, where extensive positive anomalies are imaged (Fig. 13). We observe high velocities in the transition zone beneath the western Mediterranean Basin, Italy, the Alps, the Pannonian Basin and eastern Europe. Low-rigidity material is found in the central Mediterranean Sea and the Hellenic Arc. A similar pattern has been imaged in body wave tomographic studies (e.g. Spakman *et al.* 1993; Wortel & Spakman 2000; Piromallo & Morelli 2003). The imaged seismically fast structure has been interpreted as cold subducted African lithosphere which did not penetrate into the lower mantle and lies horizontally in the transition zone. The deep structure at the edge of our model, and in particular beneath northern Africa, is not well constrained and is strongly influenced by horizontal smearing along the main path directions (Fig. 7).

8 CONCLUSIONS

We present the first regional study resolving the Eurasia–Africa plate boundary region from the Azores to the eastern Mediterranean Sea. The resolution of existing velocity models has been complemented by the temporary deployment of 25 broad-band seismic stations (MIDSEA project) along the suture zone and by using new *S* and surface waveforms recorded at permanent European seismic stations.

S-velocity models provide independent and complementary information with respect to *P*-velocity models. However, similarities

for the extensively studied continental European region between our shear wave velocity model and body wave tomographic images (e.g. Bijwaard & Spakman 2000) have been observed. As expected, due to smoothing and different data characteristics, the imaged heterogeneities in our model show a longer-wavelength character compared with *P*-velocity models. However, where the resolving power of the used data set is good, body and surface wave tomographic studies (independent data with different sensitivity) show consistent results. This lends further validity to our *S*-velocity model for regions poorly studied before, where we can achieve an unprecedented resolution (as, in particular, for the shallow mantle beneath the Mediterranean Sea, northern Africa and the eastern Atlantic Ocean).

Our *S*-velocity model shows the same order of complexity as observed at the surface: the imaged heterogeneities in the Mediterranean upper mantle correlate with the tectonics and geology along the plate boundary. The Eurasia–Africa suture zone manifests itself in the upper mantle mainly as a belt of high-velocity material representing subducted oceanic lithosphere. It can be followed to depths of 300–500 km, depending on the region and resolution. Since subduction did not occur contemporaneously throughout the region and sinking velocities are not necessarily spatially homogeneous, fragments of African lithosphere reside at different depths in the upper mantle. Where the process is still active (e.g. Crete), a continuous positive anomaly is observed from the surface down to the transition zone. At old subduction zones (e.g. Spain), detached pieces of seismically fast material are imaged at depths greater than 250 km.

In particular a new resolved feature of our *S*-velocity model is a positive anomaly imaged beneath eastern Spain between a depth of 250 and 500 km. We suggest that this fast body could be a fragment of subducted lithosphere, which detached in an early stage of northwest subduction of oceanic lithosphere in the western Mediterranean.

Not only has convergence been recorded in the upper mantle, but also extension has its own signature beneath the Mediterranean. This is particularly clear for the Algero-Provençcal and Tyrrhenian basins, where a shallow asthenospheric layer is observed.

The lithosphere–asthenosphere system of the western Mediterranean clearly differentiates itself from the structure of the older eastern Atlantic Ocean. Differences from the structure of a 4 to 20 Ma ocean are also present. These observations support the idea that, rather than a young ocean, the western Mediterranean could be a strongly stretched continent, partly affected by spreading, formed at the back of a slab. The structure characterizing the eastern Mediterranean (missing asthenospheric layer and average iasp91 uppermantle *S* velocities) suggests that this region is different from both an oceanic basin and a strongly stretched continent. The imaged structure points to a continuation of the relatively undeformed northern African continental lithosphere beneath the sea.

Major structural differences in the eastern Atlantic Ocean are imaged between the mid-Atlantic ridge and the older oceanic basins: the North Atlantic lithosphere is characterized by lower velocities beneath the spreading ridge than under the old ocean basins.

Beneath northern Africa, we imaged detached subducted lithosphere beneath northern Algeria.

In summary, EAV03 is characterized by strong contrasts between the transition zone and uppermost mantle structure. High-velocity anomalies related to fragments of subducted lithosphere have been imaged in the transition zone throughout the Mediterranean region and document its long history of subduction. The structure of the uppermost mantle is instead dominated by rapidly laterally varying low-velocity anomalies, witnessing the complex tectonic evolution of this region.

ACKNOWLEDGMENTS

We thank J. Braunmiller and F. Bernardi for providing moment tensor solutions for regional events in the Mediterranean area. We are grateful to W. Spakman for making available the global *P*-velocity model BSE_NL. We thank A. Deschamps for expert handling of and insights into the data from stations DGI, GRI, MGR, RUSF, SMPL and SOI. Th. Meier and two anonymous reviewers are acknowledged for constructive comments on the manuscript. Discussion with W. Friederich has been very helpful. Funding for this study was provided by the Swiss National Science Foundation (SNF). Financial support for the MIDSEA seismic array came from the SNF, with additional support from the Carnegie Institution of Washington, the French National Scientific Research Centre and the University of Nice at Sophia-Antipolis, the Italian National Institute of Geophysics and Volcanology and numerous local organizations (see Van der Lee *et al.* 2001). We thank the many individuals associated with MIDSEA (see Van der Lee *et al.* 2001); their support has been invaluable. EAV03 is accessible at http://www.sg.geophys.ethz.ch/midsea. Contribution number 1331 of the Institute of Geophysics, ETH Zurich.

REFERENCES

Baer, M., 1990. The seismic station network of the Swiss Seismological Service, in *International Workshop on MEDNET, the Broad-Band Seismic Network for the Mediterranean,* pp. 345–350, eds Boschi, E., Giardini, D. & Morelli, A., Istituto Nazionale Geofisica, Rome.

Bassin, C., Laske, G. & Masters, G., 2000. The current limits of resolution for surface wave tomography in North America, in *EOS, Trans. Am. geophys. Un.,* **81**(Fall Meeting Supplement), F897.

Bijwaard, H. & Spakman, W., 2000. Non-linear global *P*-wave tomography by iterated linearized inversion, *Geophys. J. Int.,* **141,** 71–82.

Blanco, M. & Spakman, W., 1993. The *P*-wave velocity structure of the mantle below the Iberian Peninsula: evidence for subducted lithosphere below southern Spain, *Tectonophysics,* **221,** 13–34.

Boschi, E., Giardini, D. & Morelli, A., 1991. MedNet: the very broad-band seismic network for the Mediterranean, *Nuovo Cimento,* **14,** 79–99.

Boschi, L., 2001. Applications of linear inverse theory in modern global seismology, *PhD thesis,* Harvard University.

Braunmiller, J., Kradolfer, U., Baer, M. & Giardini, D., 2002. Regional moment tensor determination in the European-Mediterranean region—initial results, *Tectonophysics,* **356,** 5–22.

Burrus, J. & Foucher, J., 1986. Contribution to the thermal regime of the Provençal Basin based on FLUMED heat flow surveys and previous investigations, *Tectonophysics,* **128,** 303–334.

Cammarano, F., Goes, S., Vacher, P. & Giardini, D., 2003. Inferring uppermantle temperatures from seismic velocities, *Phys. Earth planet. Inter.,* **138,** 197–222.

Carminati, E., Wortel, M., Spakman, W. & Sabadini, R., 1998. The role of slab detachment processes in the opening of the western-central Mediterranean basins: some geological and geophysical evidence, *Earth planet. Sci. Lett.,* **160,** 651–665.

Cermák, V. & Rybach, L. (ed.), 1979. *Terrestrial Heat Flow in Europe,* Springer, Berlin.

De Jonge, M., Wortel, M. & Spakman, W., 1994. Regional scale tectonic evolution and the seismic velocity structure of the lithosphere and upper mantle: the Mediterranean region, *J. geophys. Res.,* **99,** 12 091–12 108.

Dercourt, J. *et al.*, 1986. Geological evolution of the Tethys Belt from the Atlantic to the Pamirs since the Lias, *Tectonophysics,* **123,** 241–315.

Dewey, J., Helman, M., Turco, E., Hutton, D. & Knott, S., 1989. Kinematics of the western Mediterranean, in *Alpine Tectonics,* pp. 265–283, eds Coward, M., Dietrich, D. & Park, R., Blackwell Scientific, Oxford.

Dziewonski, A., Ekström, G. & Salganik, M., 1994. Centroid-moment tensor solutions for January–March 1994, *Phys. Earth planet. Int.,* **86,** 253–261.

Engdahl, E., Van der Hilst, R. & Buland, R., 1998. Global teleseismic earthquake relocation with improved traveltimes and procedures for depth determination, *Bull. seism. Soc. Am.,* **88,** 722–743.

Faccenna, C., Funiciello, F., Giardini, D. & Lucente, P., 2001. Episodic backarc extension during restricted mantle convection in the Central Mediterranean, *Earth planet. Sci. Lett.,* **187,** 105–116.

Friederich, W., 2003. The *S*-velocity structure of the East Asian mantle from inversion of shear and surface waveforms, *Geophys. J. Int.,* **153**(1), 88–102.

Grand, S., 1994. Mantle shear structure beneath the Americas and surrounding oceans, *J. geophys. Res.,* **99,** 591–621.

Hanka, W., 1990. The German Regional Broadband Seismic Network (GRN) Project, in *International Workshop on MEDNET, the Broad-Band Seismic Network for the Mediterranean,* pp. 83–95, eds Boschi, E., Giardini, D. & Morelli, A., Istituto Nazionale di Geofisica, Rome.

Hanka, W. & Kind, R., 1994. The GEOFON Program, *IRIS Newsletter,* **13,** 1–4.

Kennett, B. & Engdahl, E., 1991. Traveltimes for global earthquake location and phase identification, *Geophys. J. Int.,* **105,** 429–465.

Lloyd, S., 2003. Influence of anisotropy on 3D *S*-velocity models in the Mediterranean region, *Junior thesis*, ETH Zurich, Switzerland.

Lucente, P., Chiarabba, C., Cimini, G. & Giardini, D., 1999. Tomographic constraints on the geodynamic evolution of the Italian region, *J. geophys. Res.,* **104**(B9), 20 307–20 327.

Margheriti, L., Lucente, F. & Pondrelli, S., 2003. *SKS* splitting measurements in the Apenninic-Tyrrhenian domain (Italy) and their relation with lithospheric subduction and mantle convection, *J. geophys. Res.,* **108**(B4), 2218, doi:10.1029/2002JB0001793.

Marone, F., Van der Meijde, M., Van der Lee, S. & Giardini, D., 2003. Joint inversion of local, regional and teleseismic data for crustal thickness in the Eurasia–Africa plate boundary region, *Geophys. J. Int.,* **154,** 499–514.

Marquering, H. & Snieder, R., 1996. Shear-wave velocity structure beneath Europe, the northeastern Atlantic and western Asia from waveform inversions including surface-wave mode coupling, *Geophys. J. Int.,* **127,** 283–304.

Marquering, H., Nolet, G. & Dahlen, F., 1998. Three-dimensional waveform sensitivity kernels, *Geophys. J. Int.,* **132,** 521–534.

Martínez, M., Lana, X., Canas, J., Badal, J. & Pujades, L., 2000. Shear-wave velocity tomography of the lithosphere–asthenosphere system beneath the Mediterranean area, *Phys. Earth planet. Int.,* **122,** 33–54.

Meier, T., Lebedev, S., Nolet, G. & Dahlen, F., 1997. Diffraction tomography using multimode surface waves, *J. geophys. Res.,* **87,** 1648–1661.

Meier, T., Dietrich, K., Stöckhert, B. & Harjes, H.-P., 2003. 1-dimensional models of shear-wave velocity for the eastern Mediterranean obtained from the inversion of Rayleigh wave phase velocities and tectonic implications, submitted.

Meissner, R., Wever, T. & Flüh, E., 1987. The Moho in Europe—implications for crustal development, *Ann. Geophys.,* **5B**(4), 357–364.

Mocquet, A. & Romanowicz, B., 1990. Three-dimensional structure of the upper mantle beneath the Atlantic Ocean inferred from long-period Rayleigh waves—2. Inversion, *J. geophys. Res.,* **95**(B5), 6787–6798.

Nishimura, C. & Forsyth, D., 1989. The anisotropic structure of the upper mantle in the Pacific, *Geophys. J. R. astr. Soc.,* **96,** 203–229.

Nolet, G., 1990. Partitioned waveform inversion and 2-dimensional structure under the network of autonomously recording seismographs, *J. geophys. Res.,* **95,** 8499–8512.

Paige, C. & Saunders, M., 1982. LSQR: an algorithm for sparse linear equations and sparse least squares, *ACM Trans. Math. Software,* **8,** 195–209.

Panza, G., Mueller, S. & Calcagnile, G., 1980. The gross features of the lithosphere-asthenosphere system in Europe from seismic surface waves and body waves, *Pure appl. Geophys.,* **118,** 1209–1213.

Papazachos, C. & Nolet, G., 1997. *P* and *S* deep velocity structure of the Hellenic area obtained by robust nonlinear inversion of travel times, *J. geophys. Res.,* **102,** 8349–8367.

Paulssen, H., 1992. NARS-DEEP: NARS deployed on the East European Platform, *Europrobe News,* **1,** 9.

Piromallo, C. & Morelli, A., 2003. *P* wave tomography of the mantle under the Alpine–Mediterranean area, *J. geophys. Res.,* **108**(B2), 2065, doi:10.1029/2002JB001757.

Ritsema, J. & Van Heijst, H., 2000. New seismic model of the upper mantle beneath Africa, *Geology,* **28**(1), 63–66.

Romanowicz, B., Cara, M., Fels, J.-F. & Rouland, D., 1984. Geoscope; a French initiative in long-period three-component global seismic networks, *EOS, Trans. Am. geophys. Un,* **65**(42), 753–754.

Schmid, C., Van der Lee, S. & Giardini, D., 2004. Delay times and shear-wave splitting in the Mediterranean region, *Geophys. J. Int.,* in press.

Shapiro, N. & Ritzwoller, M., 2002. Monte-Carlo inversion for a global shear-velocity model of the crust and upper mantle, *Geophys. J. Int.,* **151,** 88–105.

Silveira, G. & Stutzmann, E., 2002. Anisotropic tomography of the Atlantic Ocean, *Phys. Earth planet. Int.,* **132,** 237–248.

Silveira, G. et al, 2002. Coordinated seismic experiment in the Azores, *Orfeus Newsletter,* **4**(2), 10.

Snieder, R., 1988. Large-scale waveform inversions of surface waves for lateral heterogeneity, 2. Application to surface waves in Europe and the Mediterranean, *J. geophys. Res.,* **93,** 12 067–12 080.

Sobolev, S., Zeyen, H., Granet, M., Achauer, U., Bauer, C., Werling, F., Altherr, R. & Fuchs, K., 1997. Upper mantle temperatures and lithosphere-asthenosphere system beneath the French Massif Central constrained by seismic, gravity, petrologic and thermal observations, *Tectonophysics,* **275**(1–3), 143–164.

Spakman, W., Van der Lee, S. & Van der Hilst, R., 1993. Travel-time tomography of the European-Mediterranean mantle down to 1400 km, *Phys. Earth planet. Int.,* **79,** 3–74.

Takeuchi, H. & Saito, M., 1972. Seismic surface waves, in *Methods in Computational Physics,* pp. 217–295, ed. Bolt, B., Academic Press, San Diego, CA.

Thio, H., Song, X., Saikia, C., Helmberger, D. & Woods, B., 1999. Seismic source and structure estimation in the western Mediterranean using a sparse broadband network, *J. geophys. Res.,* **104**(B1), 845–861.

Van der Lee, S., 1998. Observations and origin of Rayleigh-wave amplitude anomalies, *Geophys. J. Int.,* **135,** 691–699.

Van der Lee, S. & Nolet, G., 1997. Upper mantle *S*-velocity structure of North America, *J. geophys. Res.,* **102,** 22 815–22 838.

Van der Lee, S. et al, 2001. Eurasia-Africa plate boundary region yields new seismographic data, *EOS, Trans. Am. geophys. Un.,* **82**(51), 637–646.

Van der Meijde, M., Van der Lee, S. & Giardini, D., 2003. Crustal structure beneath broad-band seismic stations in the Mediterranean region, *Geophys. J. Int.,* **152,** 729–739.

Watts, A. & Torné, M., 1992. Subsidence history, crustal structure, and thermal evolution of the Valencia Trough: a young extensional basin in the western Mediterranean, *J. geophys. Res.,* **97**(B13), 20 021–20 041.

Wortel, M. & Spakman, W., 2000. Subduction and slab detachment in the Mediterranean-Carpathian region, *Science,* **290,** 1910–1917.

Yegorova, T., Starostenko, V. & Kozlenko, V., 1998. Large-scale 3-D gravity analysis of the inhomogeneities in the European-Mediterranean upper mantle, *Pure appl. Geophys.,* **151,** 549–561.

Zeck, H., 1999. Alpine plate kinematics in the western Mediterranean: a westward-directed subduction regime followed by slab roll-back and slab detachment, in *The Mediterranean Basins: Tertiary Extension within the Alpine Orogen,* pp. 109–120, ed. Durand, B., Geological Society, London.

Zielhuis, A. & Nolet, G., 1994. Shear-wave velocity variations in the upper mantle beneath central Europe, *Geophys. J. Int.,* **117,** 695–715.